The Impact of Fault Zone Plasticity on Sequences of Earthquakes and Aseismic Slip: The Role of Stress Orientation and Bulk Cohesion

Mohamed Abdelmeguid[1] and Ahmed Elbanna[1]

[1]University of Illinois at Urbana Champaign

November 30, 2022

Abstract

We present a coupled finite element spectral boundary integral framework for modeling sequences of earthquakes and aseismic slip on a 2-D planar rate-and-state fault with off-fault visco-plastic response in the plane strain approximation. The model resolves both slow aseismic deformation and inertia effects during rapid slip. We perform two sets of simulations with different choices of cohesion. The first set implements a relatively large value of the cohesion parameter, which results in limiting inelastic strain accumulation to dynamic rupture phases. The second set implements a smaller cohesion, allowing for plastic strain to accumulate in both the seismic and aseismic phases of the earthquake cycle. For the first model, our results indicate that the extent and distribution of plastic strain depend on the angle of maximum compressive principal stress. At larger angles, inelastic strain accumulates on the extensional side of a dynamically propagating rupture. At smaller angles, the extent of plasticity is limited to the compressional side of the domain. At smaller cohesion values, off-fault plasticity may occur during the aseismic phases of the earthquake cycle, which alter the nucleation and earthquake sequence pattern. Furthermore, our results at lower cohesion values indicate that plastic strain accumulation may occur in both the extensional and compressional sides of the off-fault bulk even at higher angles. This produces damage patterns that deviate from the traditional off-fault fan-like distribution observed in dynamic rupture simulations and emphasizes the significance of long-term deformation in interpreting observations.

The Impact of Fault Zone Plasticity on Sequences of Earthquakes and Aseismic Slip: The Role of Stress Orientation and Bulk Cohesion

Mohamed Abdelmeguid[1], **Ahmed Elbanna**[1]

[1]Department of Civil and Environmental Engineering, University of Illinois at Urbana-Champaign, Illinois, USA

Key Points:

- A hybrid finite element boundary integral method for earthquake cycles with off-fault plasticity in a 2-D in-plane setting.
- At higher cohesion, plasticity is limited to the co-seismic phase on the extensional side except for low angles of maximum compression.
- At lower cohesion, plasticity accumulates aseismically altering nucleation and leading to heterogeneous damage patterns.

Corresponding author: Mohamed Abdelmeguid, `meguid@illinois.edu`

Abstract

We present a coupled finite element spectral boundary integral framework for modeling sequences of earthquakes and aseismic slip on a 2-D planar rate-and-state fault with off-fault visco-plastic response in the plane strain approximation. The model resolves both slow aseismic deformation and inertia effects during rapid slip. We perform two sets of simulations with different choices of cohesion. The first set implements a relatively large value of the cohesion parameter, which results in limiting inelastic strain accumulation to dynamic rupture phases. The second set implements a smaller cohesion, allowing for plastic strain to accumulate in both the seismic and aseismic phases of the earthquake cycle. For the first model, our results indicate that the extent and distribution of plastic strain depend on the angle of maximum compressive principal stress. At larger angles, inelastic strain accumulates on the extensional side of a dynamically propagating rupture. At smaller angles, the extent of plasticity is limited to the compressional side of the domain. At smaller cohesion values, off-fault plasticity may occur during the aseismic phases of the earthquake cycle, which alter the nucleation and earthquake sequence pattern. Furthermore, our results at lower cohesion values indicate that plastic strain accumulation may occur in both the extensional and compressional sides of the off-fault bulk even at higher angles. This produces damage patterns that deviate from the traditional off-fault fan-like distribution observed in dynamic rupture simulations and emphasizes the significance of long-term deformation in interpreting observations.

Plain Language Summary

Geological observations of fault zones show that typical fault zones consist of a damaged core that has different properties from those of the surrounding host rock. These damage zones can alter the nucleation, propagation, and the timing of seismic events. Due to insufficient data, our understanding of the mechanisms for damage accumulation and evolution over an earthquake cycle remains in its infancy stage. In this article, we present a numerical framework capable of modeling the evolution of off-fault plasticity during earthquake cycles as a proxy for damage accumulation. The proposed algorithm results in computational savings. Through our framework, we investigate two different modes of plasticity accumulation; accumulation during dynamic rupture only and accumulation throughout the different phases of the earthquake cycle. The results presented predict how plasticity evolves with the accumulation of rapid and slow slip. When plasticity accumulates during both phases of the earthquake cycle, the inelastic deformations can substantially alter the nucleation and propagation of earthquake. Additionally, the damage distribution within the fault zone is more complex and heterogeneous, and may explain some unusual observations regarding off-fault damage patterns.

1 Introduction

Earthquakes are among the costliest natural hazards on Earth (D'Amico, 2016). The instabilities responsible for the onset and ensuing propagation of these events are linked to the fundamental physics of the heterogeneous and nonlinear topologically complex fault zones subjected to extreme geophysical conditions. Over sequences of seismic and aseismic slip, fault zones evolve continuously due to the feedback between nonlinear rheology, complex fault surface geometry, and long-range static and dynamic stress transfer. As there is insufficient data in the seismic catalog in the limit of large events (Lay, 2012), there is a strong need for developing computational tools that can accurately model the spatio-temporal patterns of earthquake ruptures and aseismic creep over long time scales and geologically-relevant spatial scales, in order to enable better understanding of these rare and large events, as well as aid in policy making for hazard mitigation.

Earthquake cycle simulations, also referred to as sequences of earthquakes and aseismic slip (SEAS) models, have emerged as a a promising tool for studying the long-term behavior of faults and lithospheric deformations on seismologically relevant spatio-temporal scales. They provide insight on the spontaneous nucleation and propagation of the seismic event, post-seismic response, and the aftershock sequences. For most naturally-occurring earthquakes, identifying the stress conditions that are prevailing at the onset of the seismic event is generally infeasible; thus, a need arises for simulations that would provide unbiased insight regardless of the prescribed initial conditions. This is to be contrasted with simulations of a single seismic event, in which the results depend critically on the prescribed initial stress and fault state. While in any SEAS simulation a portion of the earthquake sequence depends on the initial conditions of the system at the start of the simulation, the overall pattern would converge to a statistically steady solution independent of the initial conditions after this transitional spin-up period. The complex nature of this problem makes an analytical solution generally intractable and necessitates solving the friction-fracture problem numerically over a wide range of spatio-temporal scales to predict the nucleation, propagation, and arrest conditions of the dynamic instability (Erickson & Jiang, 2018; Jiang et al., 2022).

To alleviate the computational demand associated with modeling variable time scales, various numerical approaches have been developed to simplify the modeling process of long term history of fault slip, mostly resorting to quasi-dynamic simulations that replace inertial dynamics during rupture propagation with a radiation damping approximation (Tse & Rice, 1986; Rice, 1993; Erickson & Dunham, 2014; Hillers et al., 2006; Liu & Rice, 2007; Luo & Ampuero, 2018). Other numerical approaches involve switching between quasi-static approximation during slow deformation to a fully dynamic representation once instability nucleates (Okubo, 1989; Shibazaki & Matsu'ura, 1992; Kaneko et al., 2011; Duru et al., 2019). Lapusta et al. introduced a rigorous procedure for simulating long term evolution of slip on planar faults in a homogeneous elastic medium using a unified framework for both inertial dynamics and quasi-static inter-seismic deformation (Lapusta et al., 2000).

To address the spatial dimension of the problem, models of earthquake cycles fall under two main categories: domain-based approaches and boundary integral approaches. Domain-based methods are flexible in handling material nonlinearities and small-scale heterogeneities, as well as complexities of fault geometry (Kuna, 2013; Taborda & Bielak, 2011; Aagaard et al., 2013; Kaneko et al., 2011; Allison & Dunham, 2018; Erickson & Dunham, 2014; Thakur et al., 2020; Barbot, 2019b). However, modeling earthquake cycles with such methods is rare due to the large computational cost (Tong & Lavier, 2018; Biemiller & Lavier, 2017; Kaneko et al., 2008; Allison & Dunham, 2018; Van Dinther et al., 2013; Mckay et al., 2019; Uphoff et al., 2022). Alternatively, boundary integral techniques limit the computations to the fault plane, effectively reducing the dimensions of the problem; thus, reducing the computational cost (Aliabadi, 1997; Lapusta et al., 2000; Lapusta & Liu, 2009). However, boundary integral methods are only applicable to linear systems. Furthermore, the lack of closed-form representation for the Green's function in the majority of situations means that the ability of the method to provide well-defined solutions for domains with heterogeneities or fault roughness is compromised.

Natural faults are usually embedded in a heterogeneous bed of rocks with variable elastic properties (Lewis & Ben-Zion, 2010; Yang et al., 2011) and a potential for yielding and fracture at different thresholds (Lyakhovsky et al., 2016). Faults typically experience non-symmetric fractured inner core. Damage substantially affects local stress fields and mechanical properties of the fault zone, and contributes to energy dissipation during the earthquake cycle. Thus, despite the drawbacks, domain-based approaches remains the only candidate to modeling earthquake cycles with off-fault nonlinearities. Erickson et al (2017) modeled cycles of quasi-dynamic ruptures on vertical, planar faults in anti-plane setting and illustrated patterns of inelastic strain accumulation in the shallow regions of the fault zone. This study demonstrated the important role of off-fault plasticity on the earthquake cycle. However, the lack of wave-mediated stress transfer may alter the extent and magnitude of plasticity accumulation and consequently, the seismicity pattern. In 2-D in-plane setting (Tal & Faulkner, 2022) studies the accumulation of plasticity on both planar and rough faults and highlighted that the extent and distribution of plasticity depend on fault roughness, slip, and intensity of dynamic rupture (slip rate and rupture speed) . In their thorough analysis, (Tal & Faulkner, 2022) presented both quasi-static and dynamic models of inelasticity accumulation during earthquake cycles for a strip model with an absorbing layer, with plasticity accumulation occurring primarily during the co-seismic phase of the earthquake cycle. However, compared to the unbounded domain approximation that is more suitable for modeling the bulk surrounding crustal faults, the domain truncation involved in the strip model may quantitatively influence the quasi-static deformation field during the interseismic period as well as the wave-mediated stress transfer during the dynamic phases due to imperfect absorbing boundary conditions. To the best of our knowledge, it remains to be investigated whether the domain truncation also introduce quantitative differences on the extent and magnitude of plasticity accumulation throughout the seismic cycle.

In this paper, we present an extension of our hybrid finite element (FEM) spectral boundary integral equation (SBIE) scheme, herein referred to as FEBE, toward modeling sequence of earthquakes and aseismic slip in 2D plane strain approximation while accounting for accumulation of inelastic strains in the surrounding bulk and the inertia effects during the coseismic phase. The main idea of FEBE is to consistently couple domain and boundary based methods thus benefiting from the strengths of each scheme and minimizing the drawbacks of either one. In this framework, the region of complexity or nonlinearity is confined to a virtual strip that is discretized using finite elements. Through the consistent exchange of tractions and displacements, the virtual strip is coupled to two linearly elastic half-spaces, whereas the response of these half-spaces is modeled by SBIE. The boundary integral formulation enables us to fully account for inertial contributions during the coseismic phases of the earthquake cycle over large spatial scales at a reduced computational cost without the drawbacks associated with reduced domain size and imperfect absorbing boundary conditions.The computational efficiency of FEBE has been discussed in various previous studies (Ma et al., 2018; Abdelmeguid et al., 2019; Albertini et al., 2021).

Here we apply FEBE to investigate the effects of the initial prestress direction and the bulk yield strength on the overall sequence of earthquake and asesismic slip and the evolution of inelastic strain. While these aspects have been investigated earlier using single dynamic rupture simulations, the conclusions of these studies depend on the assumed initial conditions. It is not clear how the natural co-evolution of fault slip, stress, and off-fault plasticity, as realized through a sequence simulation, may alter these conclusions. We consider varying the angle of maximum compressive principal stress Ψ, as well as the cohesion parameter in the Drucker-Prager constitutive law and evaluate the impact of these factors on nucleation, propagation, and arrest of individual earthquake events as well as the accumulation of off-fault plasticity during seismic and aseismic phases.

The remainder of the paper is organized as follows. In Section 2, we begin by reviewing the governing equations. The hybrid numerical scheme for the in-plane formulation (FEBE) is introduced in Section 3, in which we describe the coupling with rate and state friction and off-fault inelastic rheology. Results of the simulations are reported and discussed in Section 4. We briefly discuss the implications of our results and future extensions of this initial study in Section 5. Section 6 is reserved for concluding remarks.

2 Governing Equations

We consider the two-dimensional domain Ω undergoing plane strain deformations. The domain is divided into two half spaces by , a planar, strike-slip fault interface S_f. The 2-D plane strain equations governing motion in the domain in the absence of body force are given by

$$\rho u_{\alpha,tt} = \sigma_{\alpha\beta,\beta} \quad \alpha, \beta = 1, 2 \quad \text{in} \quad \Omega \tag{1}$$

with Dirichlet boundary conditions applied on S_u and Neumann boundary conditions applied on S_T

$$u_\alpha = \bar{u}_\alpha \quad \text{on} \quad S_u \tag{2}$$

$$\sigma_{\alpha\beta} n_\beta = \bar{\tau}_\alpha \quad \text{on} \quad S_T \tag{3}$$

where u_α is the displacement vector, $\sigma_{\alpha\beta}$ is the stress tensor, ρ is material density, n_β is facing normal vector (in 2-D) from the boundary.

2.1 Linear elastic material

The stresses are given by a linear elastic constitutive law

$$\sigma_{\alpha\beta} = \lambda \delta_{\alpha\beta} \epsilon_{\gamma\gamma} + 2\mu \epsilon_{\alpha\beta} \tag{4}$$

where $\varepsilon_{\alpha\beta}$ is the infinitesimal strain tensor, and μ, and λ are the Lamé parameters. Assuming infinitesimal deformations, the strain tensor is given by

$$\epsilon_{\alpha\beta} = \frac{1}{2} \left[u_{\alpha,\beta} + u_{\beta,\alpha} \right] \tag{5}$$

2.2 Off-fault visco-plastic yielding

We consider the off-fault material response to be idealized by Drucker-Prager plasticity model. The Drucker-Prager model is closely related to the Mohr-Coulomb model but results in a smoother yield surface. It describes inelastic deformation in brittle solids arising from friction sliding of micro-cracks(Templeton & Rice, 2008). We use the Drucker-Prager plasticity model to mimic the inelastic effects from aseismic and seismic slip on small scale cracks. The yield function of the Drucker-Prager plasticity model is given by:

$$\tau_c = c\cos(\phi) - \sigma_m \sin(\phi) \tag{6}$$

for cohesion c, and internal angle of friction $\phi = \tan^{-1}(\psi)$ with bulk friction ψ and mean stress $\sigma_m = \sigma_{kk}/3$, assuming compressional stresses to be negative. Defining the second invariant of deviatoric stresses s_{ij} as

$$I_2 = \frac{1}{2} s_{ij} s_{ij} \tag{7}$$

the yield function can be then expressed as

$$F(\sigma) = \sqrt{I_2} - \tau_c \tag{8}$$

When $F(\sigma) < 0$ the material response is elastic. Plastic flow is partitioned between various components of the plastic strain rate tensor by a flow rule

$$\dot{\epsilon}^p_{ij} = \dot{\gamma}_{eq} s_{ij} / (2\sqrt{I_2}) \tag{9}$$

where, the equivalent plastic strain rate is given by $\dot{\gamma}_{eq} = \sqrt{2\dot{\epsilon}^p_{ij}\dot{\epsilon}^p_{ij}}$. The equivalent plastic strain γ_{eq} is defined through $\dot{\gamma}_{eq} = d\gamma_{eq}/dt$. The stress increment is proportional to the elastic strain increment:

$$\dot{\sigma}_{ij} = C_{ijkl}\left(\dot{\epsilon}_{ij} - \dot{\epsilon}^{p}_{ij}\right) \tag{10}$$

where, the total strain ϵ is the sum of an elastic strain component and a plastic strain component, $\epsilon_{ij} = \epsilon^{e}_{ij} + \epsilon^{p}_{ij}$, the strain is equivalent to ϵ^{e}_{ij} in case of pure elasticity.

2.2.1 Visco-plastic Regularization

An effective approach to limit the potential mesh dependence in models with perfect plasticity is to introduce a rate dependent material behavior through viscoplastic regularization. This implies that the stresses are allowed to overshoot beyond the rate-independent yield surface and subsequently relax to it over a time scale T_c. The visco-plastic response is obtained from rate-independent limit by replacing the yield condition with $F(\sigma) = \eta\lambda$, where η is the viscosity. The relaxation time is written in terms of the viscosity and the shear modulus as $T_c = \eta/(2\mu)$.

2.3 Frictional Interface

On the fault surface S_f the tractions $T^{\pm} = T^{\pm}_{o} + \triangle T^{\pm}$, relative motion $[\![u_\alpha]\!]$, and relative velocity $[\![\dot{u}_\alpha]\!]$ are defined as:

$$\triangle T^{\pm} = \triangle\sigma^{\pm}_{\alpha\beta} n^{\pm}_{\beta}, \quad [\![u_\alpha]\!] = (u^{+}_{\alpha} - u^{-}_{\alpha}), \quad [\![\dot{u}_\alpha]\!] = \frac{\partial [\![u_\alpha]\!]}{\partial t} \tag{11}$$

Imposing continuity conditions at the fault surface we obtain the following jump conditions and stress continuity conditions, these are given by

$$[\![u_1]\!] = \delta, \quad [\![u_2]\!] = \zeta \tag{12}$$

$$\triangle\sigma^{+}_{\alpha\beta} = \triangle\sigma^{-}_{\alpha\beta} \tag{13}$$

where, α is the slip, and ζ is the fault opening to be enforced in later sections. Additionally, to ensure no interpenetration we enforce that $\zeta \geq 0$.

2.3.1 Rate-and-state friction

Here, we adopt a rate and state frictional (RSF) formulation (Dieterich, 1979; Ruina, 1983) used to describe friction in tectonic settings. The boundary condition on the fault surface is enforced by equating the fault shear stress to its strength:

$$\tau = F(V,\theta) = f(V,\theta)\sigma_n \tag{14}$$

where the fault strength F is defined in terms of the effective normal stress σ_n and the friction coefficient f. In the RSF, the friction coefficient depends on the slip rate V and state θ as:

$$f(V,\theta) = f_o + a\ln(V/V_o) + b\ln(\theta V_o/L) \tag{15}$$

where L is the characteristic slip distance, f_o is the reference friction coefficient defined at a slip rate V_o. The state evolution is prescribed through the aging law (Rice & Ruina, 1983), which is commonly applied to earthquake cycle simulations (Lapusta et al., 2000; Erickson & Dunham, 2014; Herrendörfer et al., 2018; Liu & Rice, 2007) and defined as:

$$\frac{d\theta}{dt} = 1 - \frac{V\theta}{L} \tag{16}$$

This results in a steady-state solution of the state variable $\theta_{ss} = L/V$. The corresponding steady-state friction coefficient is given by:

$$f_{ss} = f_o + (a-b)\ln\left(\frac{V}{V_o}\right) \tag{17}$$

Here, the parameter combination $a-b > 0$ describes a steady state rate-strengthening frictional response (VS) and $a-b < 0$ describes a steady state rate-weakening frictional response (VW) which may lead to unstable slip and stick slip sequences.

In expression (15), the fault frictional strength becomes ill-posed at $V = 0$. There are various alternative rate and state formulations that allow for solutions near $V = 0$ (Ampuero & Ben-zion, 2008; Barbot, 2019a; Bizzarri, 2011). However, in this analysis, we follow the regularized version of the RSF presented in (Rice & Ben-Zion, 1996):

$$f(V,\theta) = a\sinh^{-1}\left[\frac{V}{2V_o}\exp\left(\frac{f_o + b\ln\left(\frac{\theta V_o}{L}\right)}{a}\right)\right] \tag{18}$$

2.3.2 Rupture nucleation and process zone

RSF introduces a length scale for the nucleation size of earthquake that may be estimated using an energy balance approach. Ampuero and Rubin (2008) established the following theoretical estimate for the nucleation size L_{nuc} for a frictional crack under slow tectonic loading (Ampuero & Rubin, 2008):

$$L_{nuc} = \frac{2\mu^* Lb}{\pi\sigma_n(b-a)^2} \tag{19}$$

where, $\mu^* = \frac{1}{1-\nu}\mu$ for mode II rupture, μ is the shear modulus, and ν is Poisson's ratio. This nucleation size defines the critical wavelength that has to be resolved within the numerical scheme and is valid for $a/b > 0.5$. In addition to the nucleation size, Dieterich presented another characteristic length scale L_b, which is associated with the process zone during the propagation of the rupture when $V\theta/L \;>>\; 1$ and scales as b^{-1} (Dieterich, 1992). The quasi-static estimate for process zone L_b is given as:

$$L_b = \frac{\mu^* L}{\sigma_n b} \tag{20}$$

It is vital to properly resolve this length scale as it is more stringent than the nucleation zone's length. For dynamic simulations, continuously resolving the process zone becomes a more challenging ordeal as its size scales with the inverse of the Lorentz factor $\gamma_L(v_r) = \sqrt{1 - v_r^2/c_s^2}$, where, v_r is rupture speed, and c_s is the shear wave speed (Freund, 1979). The dynamic process zone is given as:

$$L_b^d = A^{-1}(v_r)L_b; \qquad A_{II}^{-1} = \frac{(1-\nu)c_s^2\mathcal{D}}{v_r^2(1-v_r^2/c_s^2)^{\frac{1}{2}}} \tag{21}$$

where $\mathcal{D} = 4(1-v_r^2/c_s^2)^{\frac{1}{2}}(1-v_r^2/c_p^2)^{\frac{1}{2}} - (2-v_r^2/c_s^2)^{\frac{1}{2}}$. Note that as the rupture speed approaches the limiting wave speed the process zone $L_b^d \to 0$. In our analysis, we make sure that the process zone remains well resolved throughout the rupture history by at least 10 elements.

2.3.3 Normal stress regularization

To account for possible variations in normal stress that might occur due to the asymmetric accumulation of the plastic strain across the fault surface, we utilize a RSF formulation featuring a delayed response of the shear stress according to Prakash-Clifton law. This model fits observed frictional response better than the traditional formulation (Cochard & Rice, 2000; Ranjith & Rice, 2001). In this framework, the fault strength is given by the following (Tal et al., 2020):

$$F = f(V,\theta)\xi \tag{22}$$

The function ξ evolves exponentially with slip to the new value of σ as

$$\dot{\xi} = \frac{-V}{L_{PC}}(\xi - \sigma_n) \tag{23}$$

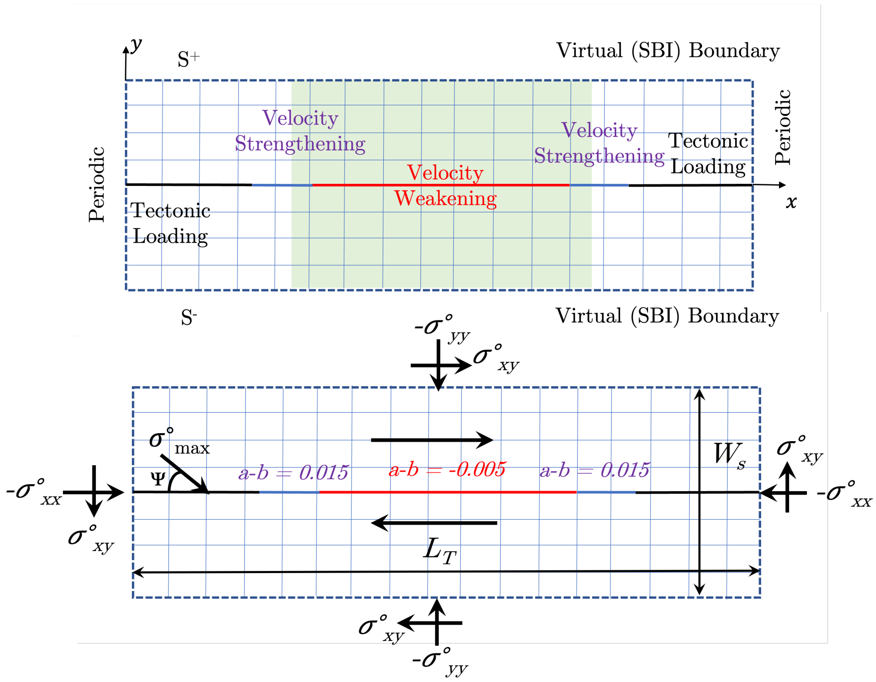

Figure 1. Schematic of the model considered in this paper (a) The computational setup for the hybrid FE-SBI scheme. A small domain adjacent to the fault surface is discretized using the finite element method. The spectral boundary integral method is used to simulate the external elastic half spaces without explicitly discretizing them by enforcing an integral relation between the slip and stresses on the virtual boundaries parallel to the fault surface. Periodic boundary conditions are used on the lateral boundaries of the domain. (b) Distribution of the fault frictional properties and background tectonic stress field.

where L_{PC} is an evolution distance of choice. In our time stepping algorithm, we consider the above equation as an additional evolution equation to compute the ξ at any given time. Here, we utilize a proportional scaling of the evolution distance relative to the characteristic length of RSF, such that $L_{PC} = 25L$. This allows for a sufficiently smooth variation in the shear stress without deviating substantially from the non-regularized version of RSF.

2.4 Geometry

We consider a planar horizontal fault governed by rate-and-state friction in the 2D plane strain approximation bisecting an unbounded elastic-visco-plastic domain with homogeneous elastic properties as shown in Figure 1a. On the fault, a potentially seismogenic patch borders regions steadily moving with a prescribed slip rate V_{pl}. The fault is slipping in a right lateral sense. We limit the FEM discretization to a domain of length L_T and width W_s (as shown in Figure 1b) . The total fault length L_T is taken to be $20L_{nuc}$, while the VW patch L_{VW} is taken to be $\sim 4L_{nuc}$. The width W_s is much smaller than the length L_T and is taken to be $0.5L_{nuc}$. The domain width W_s is always checked against the extent of the plastic strain and is taken to ensure that the FEM domain contains all the off-fault plasticity. The extent of the plastic strain is proportional to the process zone size and this guides our initial choice of the width of the virtual strip. Figure 1b further illustrates the heterogeneous spatial distribution of friction parameters to create rheological transitions on the fault surface.

3 Numerical Framework FEBE

Here, we utilize a coupled finite element and boundary element code FEBE to simulate sequence of earthquake and aseismic slip (SEAS) on a fault surface together with wave propagation in the adjacent medium. This approach was initially introduced to simulate spontaneous dynamic rupture propagation for 2-D inplane problems by Ma et al (2018) (Ma et al., 2018). and later extended to SEAS by Abdelmeguid et al. (2019) in anti-plane setting (Abdelmeguid et al., 2019). This section will outline the algorithmic development to incorporate SEAS models with off-fault inelastic bulk.

3.1 Hybrid Formulation

The hybrid formulation considered here is a combination of the finite element method (FEM) and the spectral boundary integral equation (SBIE) method. The nonlinearities, such as fault surface roughness or material nonlinearity, as well as small-scale heterogeneities, are confined apriori in a virtual strip of a certain width. This virtual strip is then discretized and modeled using FEM. The rest of the domain, which is homogeneous and linear-elastic, is modeled using the SBIE method as two half-spaces and coupled to the FEM domain on each side (S^+, S^-). The two methods enforce continuity by exchanging traction and displacement boundary conditions at those sides. The general setup of the hybrid method is shown in Figure 1a. The width of the virtual strip depends on the nature of the problem and may be adjusted to contain the heterogeneities, nonlinearities, and other fault zone complexities. Details on the individual formulation of FEM and SBIE is provided in Appendix A and Appendix B respectively.

3.2 Time Stepping

We consider simulations of long sequence of earthquakes and aseismic slip during which the fault is stressed gradually through tectonic load V_{pl} on the edges of the seismogenic patch. During the inter-seismic phase this results in the accumulation of aseismic slip predominantly within the creeping VS regions and regions of rheological transition. The accumulation of aseismic slip result in stress concentration that spontaneously nucleate an earthquake within the VW patch consistent with the frictional law and bulk material response. Here, we utilize a quasi-dynamic approximation during periods of aseismic slip and switch to fully dynamic approach during the dynamic rupture period. This limits the stringent conditions imposed by stability condition on the time step during the periods of slow tectonic loading. During the quasi-dynamic periods we utilize an adaptive time marching scheme proposed by (Lapusta & Rice, 2003). The time step during dynamic rupture periods is chosen to satisfy the Courant–Friedrichs–Lewy (CFL) condition (Courant et al., 1928).

We switch between quasi-dynamic and fully dynamic solvers based on the value of the maximum slip rate. For the problem discussed below we switch from quasi-dynamic scheme to a dynamic scheme based on a threshold $V^{QD} = 1$ mm/s , and from dynamic to quasi-dynamic based on a threshold $V^{DQ} = 0.8$ mm/s. To evaluate the role of transition threshold, we estimate the ratio between radiation damping term given as $\eta^{RD}V$, where $\eta^{RD} = \mu/2c_s$ and quasi-static shear stress τ_{qs}. Neglecting the inertia effects is justifiable as long as the magnitude of the radiation damping term is relatively small which is ensured by having the ratio $R = \eta^{RD}V/\tau_{qs}$ much smaller than unity $R << 1$. The above thresholds ensure that ratio $R < 10^{-4}$. Furthermore, we have performed numerical tests to confirm that the accuracy of the obtained results are independent of the threshold choice, as long as it is small enough as outlined above.

3.3 Quasi-dynamic Algorithm

Here, we outline the quasi-dynamic modeling framework where inertial effects are approximated with a radiation damping term when resolving shear tractions on the fault surface. Thus, time dependence enters through the constitutive model and the loading conditions only. It is important to note that this approximation is valid only when inertial effects are sufficiently small.

Time marching within the quasi-dynamic algorithm based on FEM descritization requires solving the following system of equations at every time-step

$$\mathbf{K}u(t) + \mathbf{L}_s^T \tau^{SBI}(t) + \mathbf{L}^T T^f(t) = \mathbf{F}(t) \tag{24}$$

$$\mathbf{L}u(t) = \mathbf{D}(t) \tag{25}$$

where, $\tau^{SBI}(t)$ represent the action of the elastic half-spaces modelled using SBIE on the finite element strip. In the quasi-static limit, the tractions on the virtual boundary nodes depend entirely on the corresponding displacement. We detail the implementation of SBIE in the limit of quasi-static deformations in Section 3.3.1.

3.3.1 Quasi-static implementation of SBIE

Within the SBIE framework, the relationship between the traction τ_i and resulting displacements is given as:

$$\tau_i^{\pm}(x_1, t) = \tau_i^{0\pm}(x_1, t) \mp \eta_i^{RD} \dot{u}_i^{\pm}(x_1, t) \pm f_i^{\pm}(x_1, t) \tag{26}$$

In the quasi-static limit expression (26) reduces to

$$\tau_i^{\pm}(x_1, t) = \tau_i^{0\pm}(x_1, t) \pm f_i^{\pm}(x_1, t) \tag{27}$$

With the convolution terms $f_i(x_1, t)$ depending on $u(x_1, t)$. Breitenfeld and Geubelle (1998) provided closed form expression for Fourier coefficients $F_i(t; q)$ of the convolution term based on a displacement representation (Breitenfeld & Geubelle, 1998). Through integration by parts we can extract the static contributions from the convolution integral such that in the quasi-static limit the $F_i(t; q)$ reduces to:

$$F_1^{\pm}(t; q) = \mp\mu^{\pm}|q|\mathcal{C}_{11}U_1^{\pm} + \left(i\left[2 - \left(\frac{c_p^{\pm}}{c_s^{\pm}}\right)\right]\mu^{\pm}q + i\mu^{\pm}q\mathcal{C}_{12}\right)U_2^{\pm} \tag{28}$$

$$F_2^{\pm}(t; q) = \mp\mu^{\pm}|q|\mathcal{C}_{22}U_2^{\pm} - \left(i\left[2 - \left(\frac{c_p^{\pm}}{c_s^{\pm}}\right)\right]\mu^{\pm}q + i\mu^{\pm}q\mathcal{C}_{12}\right)U_1^{\pm} \tag{29}$$

where, $\mathcal{C}_{ij}$ are the integrated convolution kernels. We can write the coefficients in In a more compact form $F_i^{\pm}(t; q) = \mathcal{Q}_{ij}^{\pm}U_j^{\pm}(t; q)$, where, $\mathcal{Q}$ represent a projection that depends on the material properties μ, c_p/c_s and wave number q . Through the Discrete Fourier transform we represent the convolution term $f_i(x_1, t)$ as a Fourier series:

$$f_i^{\pm}(x_1, t) = \sum_{q=-N/2}^{N/2} F_i^{\pm} e^{ik_q x_1}, \quad k_q = \frac{2\pi q}{\lambda_s} \tag{30}$$

where, λ_s is the size of the virtual boundary under consideration. We substitute expressions (28) and (29) into expression (30) to obtain

$$f_i^{\pm}(x_1, t) = \sum_{q=-N/2}^{N/2} \mathcal{Q}_{ij}^{\pm}U_j^{\pm} e^{ik_q x_1}, \quad k_q = \frac{2\pi q}{\lambda_s} \tag{31}$$

Using inverse Fourier transform provide

$$f_i^{\pm}(x_1,t) = \sum_{q=-N/2}^{N/2} \mathcal{Q}_{ij}^{\pm} \left(\frac{1}{N} \sum_{p=-N/2}^{N/2} u_j e^{-ik_p q} \right) e^{ik_q x_1} \tag{32}$$

In the above form, the expressions permits a representation of convolution term $f_i(x_1,t) = A_{ij}u_j$. We note, that despite $\mathcal{Q}_{ij} = \mathbf{0}$ at $q=0$, the resultant A_{ij} operator is non-singular due to the inverse transform operation. Thus, the tractions on the spectral boundary nodes can be written in terms of the displacements on the interface nodes between FE and SBI domain such that $\mathbf{L}_s^T \tau^{SBI}(t) = \tilde{\mathbf{K}}u(t)$, where $\tilde{\mathbf{K}} = \mathbf{L}_s^T\mathbf{A}$ represent the quasi-static stiffness from the halfspace acting on the finite element domain, and $u(t)$ represent the displacement on the virtual boundaries.

3.3.2 Coupled FE-SBI

Given the explicit representation of the SBI tractions in terms of displacement we can readily amend the system of equations given in expressions (24), and (25)

$$\left[\mathbf{K} + \tilde{\mathbf{K}}\right] u^n + \mathbf{L}^T T^{f,n} = \mathbf{F}^n \tag{33}$$

$$\mathbf{L}u^n = \mathbf{D}^n \tag{34}$$

We express the system of equations given by equations (33), and (34) as $\mathbf{A}\underline{\mathbf{x}} = \mathbf{b}$. Accordingly, the algorithm for coupled FE-SBI system becomes:

1. We solve the quasi-static system of equations for $u(t)$, and $T^f(t)$ subjected to prescribed slip $\delta(t)$. Now given as:
$$\mathbf{A}\underline{\mathbf{x}}^n = \mathbf{b}^n \tag{35}$$
2. We solve RSF given in expression (14) using a safegaurded Newton Raphson approach for slip rate $V(t)$ given fault traction $T^{f,n}$.
3. Predict a new stable time increment using Lapusta et al (2000) criterion such that $\triangle t = \chi L/V^n$, where χ is a constant that depends on the frictional parameters and stability considerations as noted in (Lapusta et al., 2000)
4. We use V^n to update slip d and state variable θ as follows:

$$\delta^{n+1} = \delta^n + \triangle t V^n \tag{36}$$

$$\theta^{n+1} = \theta^n + \triangle t\left(1 - \frac{V^n\theta^n}{L}\right) \tag{37}$$

5. Return to Step 1 to advance to the next time step

3.4 Dynamic Algorithm

When neglecting inertial effects is no longer justifiable, we transition to a fully dynamic algorithm. Here, we outline the dynamic rupture framework we utilize within FEBE

3.4.1 Finite element

The step-by-step time integration approach is a central-difference explicit formulation and follows:

$$\dot{u}^{n+1/2} = \dot{u}^{n-1/2} + \triangle t M^{-1}(T^n - f^n) \tag{38}$$

$$u^{n+1} = u^n + \triangle t \dot{u}^{n+1/2} \tag{39}$$

where ($\dot{}$) represent the partial derivative with respect to time and superscript n indicates the time step index. A lumped mass matrix is used which eliminates the need to form a global stiffness matrix; therefore, these are all nodal values and the subscript i is omitted. f is the internal force due to the deformation of the solid and $\triangle t$ the time step. The time stepping of the algorithm must satisfy the stability constraints of the Courant-Friedrichs-Lewy (CFL) condition. Along the frictional interface the expression balance of linear momentum yield

$$\dot{u}^{n+1/2} = \dot{u}^{n-1/2} + \triangle t M^{-1}(T_f^n - f^n) \tag{40}$$

The computation of frictional tractions T_f at the interface is based on RSF framework and imposed on the fault using the traction-at-split node (TSN) method.

3.4.2 Spectral boundary integral method

The time integration scheme used in the SBI is explicit and is given by sampling

$$u_i^{\pm n+1} = u_i^{\pm n} + \triangle t \dot{u}_i^{\pm n} \tag{41}$$

where the velocity is found by solving expression 26, which results in

$$\dot{u}_1^{\pm n} = \pm \frac{c_s}{\mu} \left(f_1^{\pm n} - \tau_1^{\pm n} + \tau_1^{\pm o} \right) \tag{42}$$

$$\dot{u}_2^{\pm n} = \pm \frac{c_p}{\lambda + 2\mu} \left(f_2^{\pm n} - \tau_2^{\pm n} + \tau_2^{\pm o} \right) \tag{43}$$

3.4.3 Coupled FE-SBI

To couple the two schemes we apply a staggered coupling approach, in which the FEM and SBI share nodes at the boundary of the virtual strip. The shared nodes are part of the displacement boundary of the FEM. While FEM provides SBI with the tractions along the virtual boundary, SBI returns the displacement that is to be imposed on S_{SBI} of FEM. The detailed step-by-step procedure is as follows:

1. Solve full time step within the FEM by solving equations (38) and (39).
2. Set interface tractions in the SBI equal to the internal forces from the FEM: $\tau_i^{n,SBI} = f_i^{n,FEM}$, where f_i^n is obtained by solving for internal forces.
3. Solve full time step within SBI by solving expressions (42) and (43) .
4. Set the displacements on the shared notes in FEM to displacements from SBI: $u_i^{n+1,FEM} = u_i^{n+1,SBI}$.
5. Return to Step 1 to advance to the next time step

3.5 Implementation of the visco-plastic response

We use a Return Mapping algorithm, following Simo and Hughes (1998), to implement the visco-plastic response of the bulk. In expression (10) we introduced the additive decomposition of the total strain into an elastic and a plastic component. This yields a modification to the system of equations (24), and (25) such that viscoplasticity contribution is described using a forcing term denoted $\mathbf{F}^p$ and the discretized system of equations becomes:

$$\mathbf{M}\ddot{u}^n + \mathbf{K}u^n + \mathbf{L}_s^T \tau^{SBI,n} + \mathbf{L}^T T^{f,n} = \mathbf{F}^n + \mathbf{F}^{p,n} \tag{44}$$

where, $\mathbf{F}^p$ is computed at an element level based on the stress state and yield criterion and then assembled globally. The algorithm for computing $\mathbf{F}^p$ is given in Algorithm (1). The predicted plastic forces are appended to both quasi-dynamic and dynamic algorithms. Noting that in the quasi-dynamic sense, iterations may be necessary for global equilibrium as demonstrated in Algorithm (2).

Algorithm 1 Off-fault plasticity algorithm

Require: Degrees of freedom u^n
Ensure: Computes $\mathbf{F}^{p,n}$
for $s \leftarrow N$ downto 1 **do**
  Compute $\sigma^n_{s,trial}$, assuming $\epsilon^{vp,n}_s = \epsilon^{vp,n-1}_s$ ▷ purely elastic material response;
  $F^n_{s,trial} \leftarrow \sqrt{I^n_{2,s,trial}} - \tau^n_{c,s,trial}$
  if $F^n_{s,trial} \leq 0$ **then**
    $(\quad)^n \leftarrow (\quad)^n_{trial}$;
    $\mathbf{F}^{p,n}_s \leftarrow \mathbf{F}^{p,n-1}_s$;
  else
    $\mathbf{n}^n \leftarrow \mathbf{s}^n_{trial} / \sqrt{I^n_{2,trial}}$
    $\triangle\epsilon^{vp} \leftarrow \left[F^n_{trial} / \left(\frac{\eta}{\triangle t} + 2\mu\right)\right] \mathbf{n}^n$
    $\epsilon^{vp,n} \leftarrow \epsilon^{vp,n-1} + \triangle\epsilon^{vp}$
    $\mathbf{s}^n \leftarrow \mathbf{s}^n_{trial} - 2\mu\triangle\epsilon^{vp}$
    $\mathbf{F}^{p,n}_s \leftarrow \int_{V_s} \nabla N^T_s \cdot \mathbf{C}\epsilon^{vp,n} dV_s$
  end if
end for
$\mathbf{F}^p_{n+1} \leftarrow \mathrm{A}^N_{s=1} \mathbf{F}^p_{s,n+1}$ ▷ Assemble the global plastic force;

Algorithm 2 Quasi-dynamic algorithm

Require: Degrees of freedom δ^n, θ^n and time t
Ensure: Computes δ^{n+1} and θ^{n+1}
$\mathbf{F}^{p,n}_k \leftarrow \mathbf{F}^{p,n-1}$ ▷ Purely elastic
Solve

$$\left[\mathbf{K} + \tilde{\mathbf{K}}\right] u^n_k + \mathbf{L}^T T^{f,n}_k = \mathbf{F}^n + \mathbf{F}^{p,n}_k$$

$$\mathbf{L}u^n_k = \mathbf{D}^n$$

Compute $\mathbf{F}^{p,n}_{k+1}$ using Algorithm 1 and u^n_k.
if $F^{p,n}_{k+1} = F^{p,n}_k$ **then** ▷ No plasticity accumulated
  $u^n \leftarrow u^n_k$;
  $T^{f,n} \leftarrow T^{f,n}_k$;
else
  while $er \geq$ tol **do**
    $F^{p,n}_k \leftarrow F^{p,n}_{k+1}$
    Solve

$$\left[\mathbf{K} + \tilde{\mathbf{K}}\right] u^n_k + \mathbf{L}^T T^{f,n}_k = \mathbf{F}^n + \mathbf{F}^{p,n}_k$$

$$\mathbf{L}u^n_k = \mathbf{D}^n$$

    Compute $\mathbf{F}^{p,n}_{k+1}$ using Algorithm 1 and u^n_k.
    $er \leftarrow ||u^n_k - u^n_{k-1}|| / ||u^n_k||$
  end while
  $u^n \leftarrow u^n_k$;
  $T^{f,n} \leftarrow T^{f,n}_k$;
end if
Solve $\tau^n - f(V^n, \theta^n)\sigma_n = 0$ for V^n
$\triangle t \leftarrow \chi L / V^n$
$\delta^{n+1} \leftarrow \delta^n + \triangle t V^n$
$\theta^{n+1} \leftarrow \theta^n + \triangle t \dot{\theta}^n$

Table 1. Parameters description

Medium Parameter	Symbol	Value
Shear wave speed (km/s)	c_s	3.2
Pressure wave speed (km/s)	c_p	5.5
Density (kg/m^3)	ρ	2670.0
Length of the domain (m)	L_T	150
Distance between two virtual boundaries (m)	W_s	varies
Angle of Internal Friction	ϕ	31.6°
Cohesion (MPa)	c	47 and 25
Angle of Maximum Compressive principal stress	Ψ	varies
Viscosity term (GPa-s)	η	2.73
Background Stress	**Symbol**	**Value**
Background Vertical Stress (MPa)	σ_{yy}	100
Background Horizontal Stress (MPa)	σ_{xx}	varies
Background Shear Stress (MPa)	σ_{xy}	56
Fault Parameters	**Symbol**	**Value**
Static Coefficient of friction	f_o	0.6
Critical slip distance (μm)	L	50
Reference velocity (m/s)	V_o	10^{-6}
Tectonic loading (m/s)	V_{pl}	10^{-9}
Width of VW patch (m)	L_{VW}	30
Width of transition (m)	L_{VW-VS}	5
Width of the fault (m)	L_f	90
Evolution effect parameter	b	0.015
Steady state velocity dependence in VW patch	$(a_{VW} - b)$	-0.005
Steady state velocity dependence in VS patch	$(a_{VS} - b)$	0.015
Nucleation size (m)	L_{nuc}	6.96
Quasi-static process zone size (m)	L_b	1.2
Grid size (m)	$\triangle x$	0.1

4 Application

In this initial study, we use FEBE to explore the co-evolution of fault slip and off-fault inelastic deformation through long sequences of earthquakes and aseismic slip. Specifically, we investigate the role of yield stress and the angle of maximum compressive stress on the plasticity accumulation and seismicity patterns. Through varying cohesion within the Drucker-Prager yield criterion, we consider two cases: Case (I) cohesion $c = 47$ (MPa) and Case (II) cohesion $c = 25$ (MPa). The high cohesion in the first case limits the plasticity accumulation to the dynamic rupture phase of the earthquake cycles. The lower cohesion in the second case enables plasticity to occur during the aseismic phase in addition to the co-seismic plasticity. Within each case we explore a parameter space of varying angle of maximum compressive principal stress to investigate the role of the tectonic setting. Other parameters used in the simulations are listed in Table 1.

4.1 Case (I) : High cohesion $c = 47$ (MPa)

Figure 2 illustrates the off-fault equivalent plastic strain for case (I) with $c = 47$ (MPa) at various angle of maximum compressive principal stress Ψ after 11 seismic events.

Figure 2a-d show that for angles between $25°-45°$ as the angle of maximum compressive principal stress increases, the plasticity accumulation occurs primarily in the extensional side of the fault. Throughout the sequence, the nucleation side remains the same and is highlighted with a yellow star. Figure 2d demonstrate that at $\Psi = 45°$ plastic deformation spans almost the entire propagation distance, while for $\Psi = 35°$ the extent of plasticity is $\sim 1.25L_{nuc}$, and only $\sim 0.5L_{nuc}$ for $\Psi = 25°$. For $\Psi = 15°$ (shown in Figure 2a) the plastic strain accumulation shifts primarily to the compressional side, and plasticity extends over a significant portion of the fault length. However, we still observe some plastic deformations in the extensional side toward the end of the rupture propagation length. The shifting of the preferred fault side for plastic strain accumulation with Ψ is consistent with the observations presented in (Templeton & Rice, 2008; Dunham et al., 2011) based on simulations of individual dynamic ruptures. Observing the same pattern in the sequence simulation is thus expected as long as the plastic strain accumulation during the inter-seismic period is negligible.

To explore the plasticity accumulation during different intervals of the earthquake cycle, Figure 3 demonstrates the plastic strain accumulation during selected individual earthquake events for $\Psi = 45°$. Figure 3a shows the extent and magnitude of equivalent plastic strain during the first event. There, the plasticity is localized primarily within the extensional side close to the hypocenter of the event. Next, Figure 3b shows the equivalent plastic strain during the fifth event which exhibits a longer extent of accumulation spanning the entirety of the fault length. Here, the plastic strain is also accumulating on the extensional side. Finally, Figure 3c shows that, at later stages, the magnitude and extent of accumulation remains similar as the system evolves to a new steady state.

4.2 Case (II) : Low cohesion $c = 25$ (MPa)

To investigate the role of the bulk yield strength we considered case (II) with a lower cohesion $c = 25$ (MPa). This choice of cohesion enables plastic strain accumulation during both the aseismic and coseismic phases of the sequence simulation. Other than the different value of the cohesion parameter, all the bulk and interfacial properties are the same as case (I). Figure 4 illustrates the accumulation of inelastic strain after 11 events for various angles of the initial maximum compressive principal stress Ψ from $25°$ to $45°$. Similar to case (I) we observe that the spatial extent and magnitude of the equivalent plastic strain decrease as the angle of the maximum compressive stress Ψ decreases. Furthermore, for all three angles, we observe localized accumulation of in-elasticity near the center of the fault spanning $-0.5 < x/L_{nuc} < 0.5$. However, in contrast to case (I) the accumulation of equivalent plastic strain is not limited to the extensional side of the fault. Rather, it appears to be distributed within the four quadrants. For $\Psi = 45°$ shown in Figure 4c the total plastic strain accumulated after 11 events appears to be concentrated more on the compressional side of the fault when evaluated based on the sense of slip in the most recent earthquake event whose nucleation site is highlighted with the circle. This apparently paradoxical result is explained as follows.

We start by pointing out that the terms "compressional" and "extensional" are used to refer to the signs of the fault-parallel strain ϵ_{xx} along the fault walls near the rupture front during the dynamic phase as shown in Figure 5b. During earthquake sequence simulations, this designation maybe revisited to account for the role of aseismic creep. A more general definition is based on the first motion experienced in the material surrounding the fault and that may indeed differ throughout the seismic cycle depending on the location of the hypocenter and the direction of propagation of slip during the aseismic and seismic phases. Consider, for example, the aseismic motion associated with the creeping front penetrating the VW patch from the left (shown in Figure 5a). During this aseismic phase, the first motion associated with the creeping fronts propagating toward the locked center of the fault is such that the extensional side is on the lower left quadrant of the domain while the compressional side is on the upper left quadrant. Accordingly,

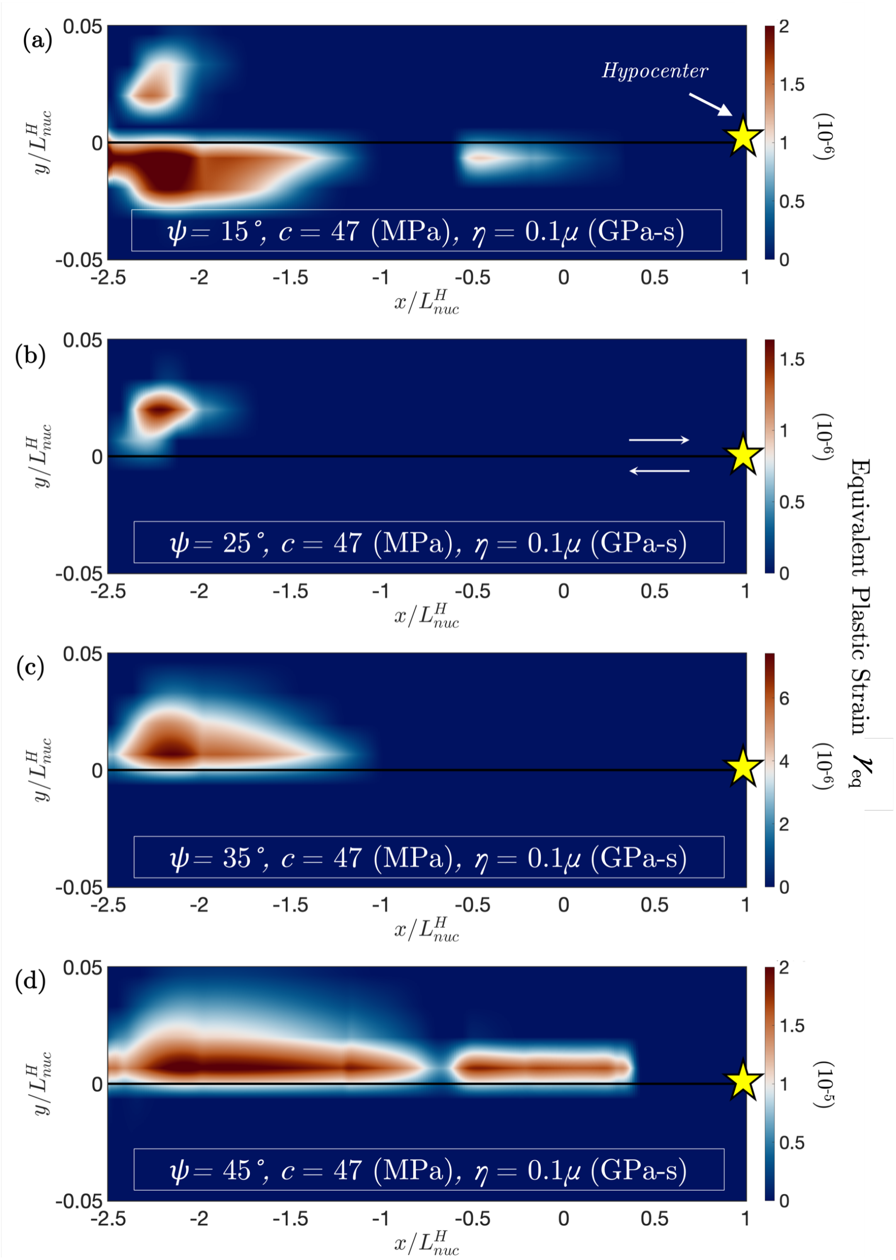

Figure 2. The magnitude and extent of the equivalent plastic strain for case (I) model at various angles of maximum compressive principal stress Ψ after 11 events. (a) $\Psi = 15°$, (b) $\Psi = 25°$, (c) $\Psi = 35°$, and (d) $\Psi = 45°$. The yellow star indicates the hypocenter of earthquake sequences beyond the first event. The contour colors indicate the magnitude of the equivalent plastic strain.

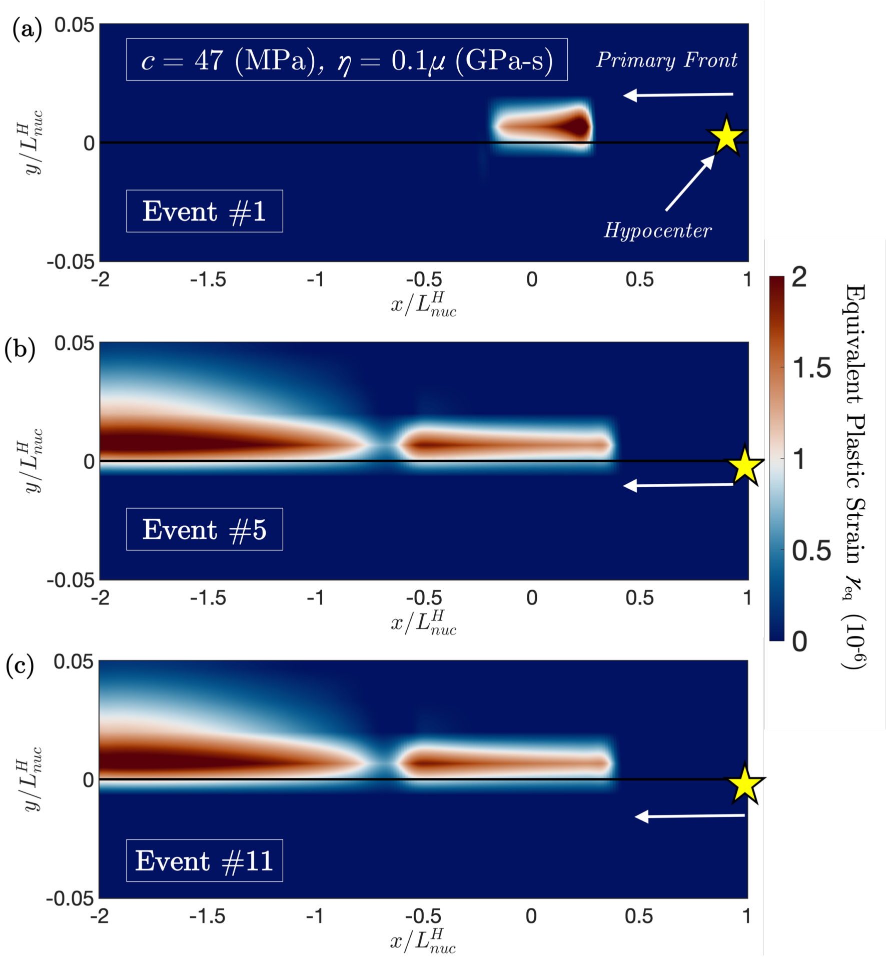

Figure 3. The magnitude and extent of the equivalent plastic strain at different intervals of the earthquake cycle. (a) During the first event, (b) During the fifth event, and (c) During the eleventh event. The yellow star indicates the hypocenter of the event. The contour colors indicate the magnitude of the equivalent plastic strain.

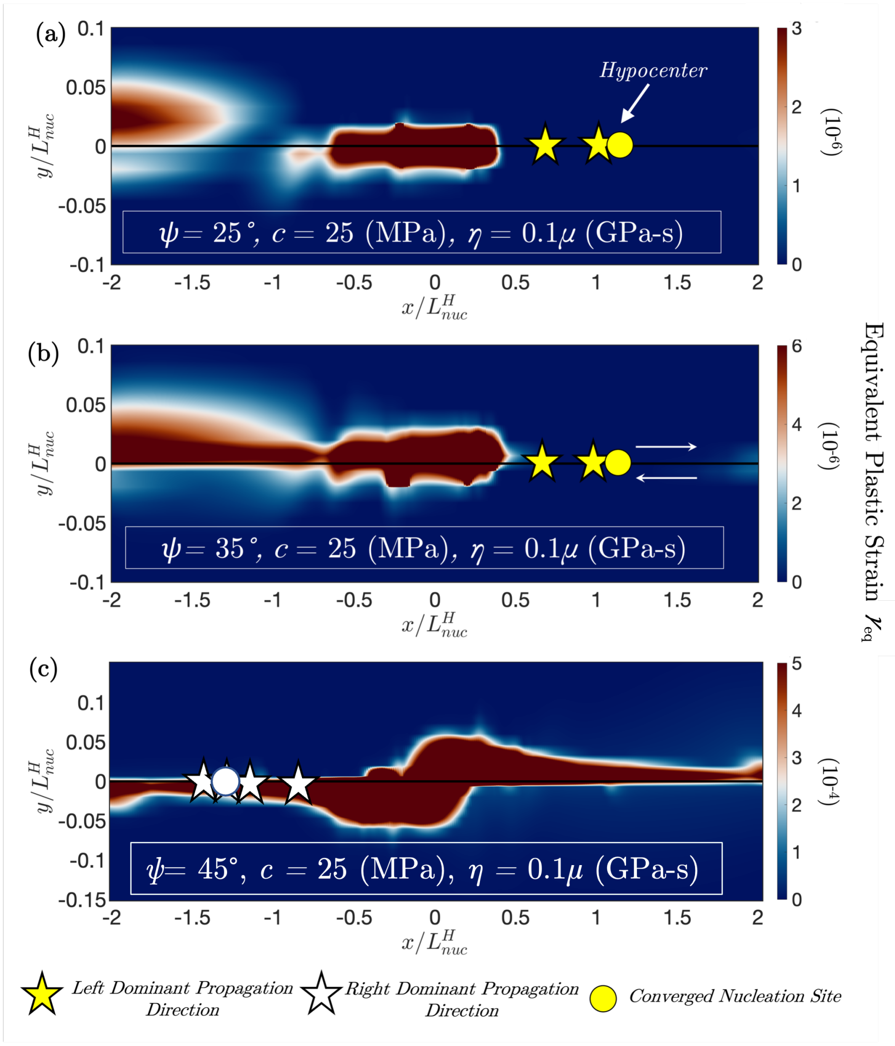

Figure 4. The magnitude and extent of the equivalent plastic strain for case (II) model at various angles of maximum compressive principal stress Ψ after 8 events. (a) $\Psi = 25^\circ$, (b) $\Psi = 35^\circ$, (c) $\Psi = 45^\circ$. The star marker indicates hypocenters for earthquake events, yellow color indicates a left dominant propagation direction, a white color indicates a right dominant propagation direction. The circle indicates the converged nucleation site after the initial phases. The contour colors indicate the magnitude of equivalent plastic strain.

we expect plastic strain accumulation associated with this front to occur preferentially within the lower left quadrant. The opposite is true for the creeping front penetrating the VW region from the right (shown in Figure 5c). The plastic strain accumulation associated with the dynamic rupture in any of the subsequent events will depend on the nucleation site and the dominant propagation direction. It may or many not agree with the plasticity accumulation during the prior aseismic phase or previous seismic events. Thus, the cumulative plastic strain reflects a rich evolutionary process and it may be challenging to decouple the observed damage pattern from the full deformation history.

To further explore the mechanism of plasticity accumulation within the different phases of the earthquake sequence, Figure 6a-c shows the plastic strain accumulation during selected individual earthquake events and interseismic periods. Figure 6a illustrates

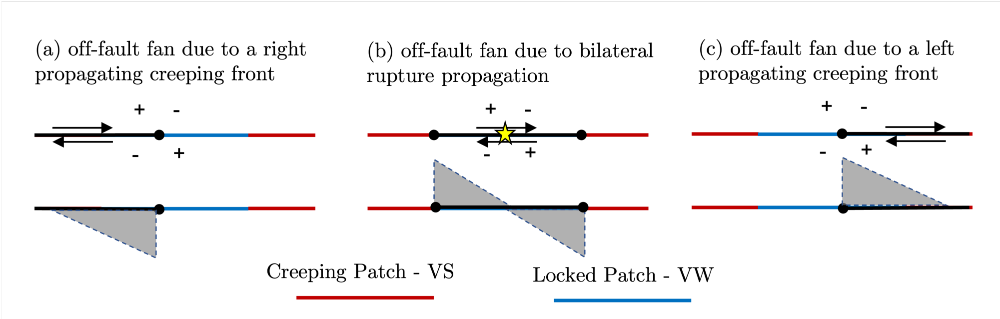

Figure 5. Schematic of off-fault plastic strain accumulation patterns developing at the tip of a sliding strike-slip fault (a) Plasticity accumulation due to a right propagating creeping front. (b) Plasticity accumulates in the extensional side of the off-fault bulk at higher Ψ values during dynamic rupture. (c) Plasticity accumulation due to a left propagating creeping front. The tip of the propagating fronts is highlighted with a black circle. The hypocenter of the dynamic rupture is highlighted with a yellow star.

the equivalent plastic strain accumulation that occurred during the second event of the earthquake sequence. The accumulation is primarily localized within the extensional side of the fault during rupture propagation, with substantial localization near the hypocenter which occurs during the bilateral nucleation phase of the event. However, unlike in case (I), at longer distances the accumulation starts to expand into the compressional side at $x/L_{nuc} > 1$. Similarly for events 4 and 8 the inelastic strain accumulation occur on the extensional side when measured relative to the rupture propagation, with expansion to the compressional side at longer propagation distances. This observation, in conjunction with the absence of plasticity accumulation within the compressional quadrant during dynamic rupture for case (I), suggests that aseismic plastic strain accumulation plays a role in altering the stress state in the bulk allowing for plasticity to accumulate in a heterogeneous pattern.

To gain further insight on how plasticity accumulates during the aseismic phases, we focus on the case of $\Psi = 45°$. Figure 6d-f illustrates the equivalent plastic strain accumulation between different earthquake events. 6d in particular demonstrate the aseismic inelastic strains accumulated prior to the first event. We observe that a significant portion of the total plastic strain (shown in Figure 4c) is accumulated during this stage. Plasticity accumulation during aseismic periods decrease substantially between event 4 and 5 as shown in Figure 6e, and becomes almost negligible between event 7 and event 8. However, off-fault yielding during these aseismic phases affects the deformation pattern leading to changes in the bulk normal stress distribution in the surrounding domain. An increase in the normal stress due to the stress redistribution associated with aseismic plasticity results in a increase in the bulk yield strength within the aseismic plastic zone.

To explain the unexpected shift of plasticity accumulation into the compressional side at longer propagation distance, in Figure 7 we plot the mean stress, and shear stress fields in addition to equivalent plastic strain accumulated for case (II) during event 4 of the cycle at different times $t = 0.036$, and 0.065 seconds. Figure 7a demonstrates the heterogeneous mean stress field due to the asesimic plasticity accumulation in prior history. Particularly, we observe that the aseismic creep results in a lower background mean stress within the bulk compressional quadrants except for regions that accumulated plasticity during earlier aseismic phases. During the dynamic rupture phase, the lower cohesion coupled with lower background mean stress results in lower yield stress ahead of

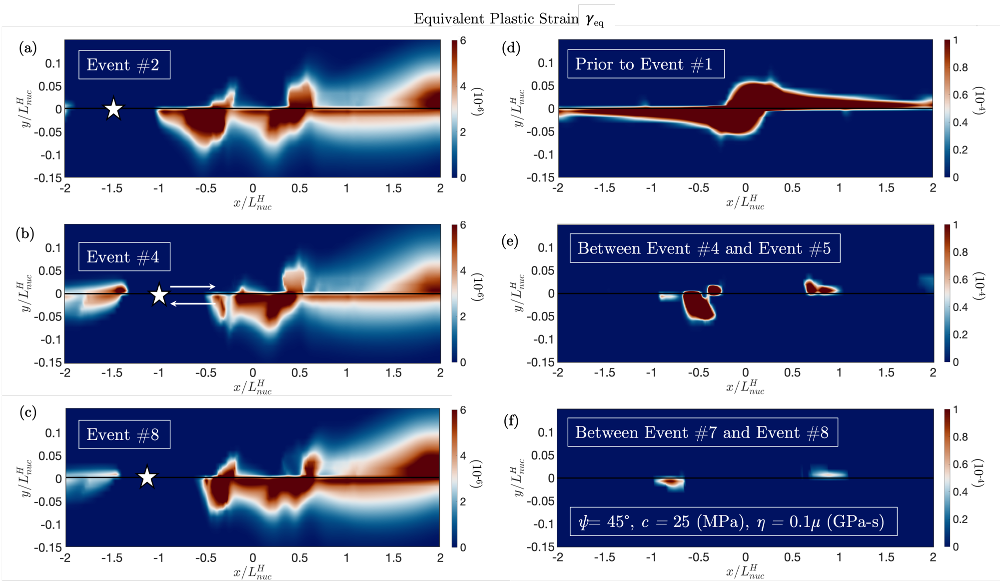

Figure 6. The magnitude and extent of the equivalent plastic strain for case (II) model at $\Psi = 45°$ at different stages of the earthquake cycle. (a) During the second event of the cycle showing localization in both the extensional and compressional sides. (b) During the fourth event of the cycle. (c) During the eighth event of the cycle. (d) Prior to the first event showing substantial plasticity accumulation during the first aseismic phase. (e) Between the end of the fourth event and the start of event five. (f) Between the end of the seventh event and the start of event eight, demonstrating negligible plasticity accumulation during the aseismic phase at later time in the earthquake cycle. Yellow star indicates the hypocenter of the earthquake event. Contour colors indicate the magnitude of equivalent plastic strain.

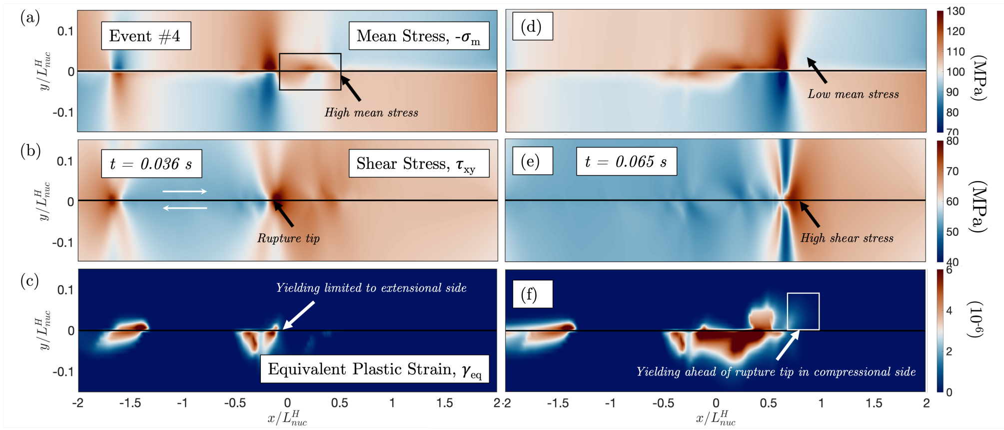

Figure 7. Contours of mean stress, shear stress, and equivalent plastic strain during event 4 shown for case (II) model at $\Psi = 45°$ at different time intervals $t = 0.036$, and 0.065 seconds. (a) Mean stress distribution at $t = 0.036$ seconds highlighting the increased background stress within the aseismic plastic region. (b) Shear stress at at $t = 0.036$ seconds. (c) Equivalent plastic strain accumulated during the event up to $t = 0.036$ seconds only limited to extensional side quadrant. (d) Mean stress distribution at $t = 0.065$ seconds highlighting the reduced background stress ahead of the rupture tip. (e) Shear stress at at $t = 0.065$ seconds. (f) Equivalent plastic strain accumulated during the event up to $t = 0.065$ seconds due to lower cohesion and mean stress the plasticity starts to accumulate within the compressional side.

the rupture tip. Accordingly, plasticity accumulation within the compressional quadrant becomes feasible as the shear stress increase with propagation distance. We mainly attribute the early delay in the accumulation of inelastic strains within the compressional quadrant (as shown in Figure 6b) to the high mean stress values within the region of accumulated plasticity prior to event 4 as highlighted in Figure 7b at $t = 0.036$ seconds. Within that region, Figure 7c shows that plasticity accumulates primary in the extensional quadrant as rupture propagates. In contrast, at later times, as the rupture propagates away from the high mean stress regions (see Figure 7d), and the shear stress magnitude increases with rupture propagation (see Figure 7e), the stress state ahead of the rupture tip favors yielding. Thus, we observe in Figure 7f that plasticity starts to accumulate ahead of the rupture tip within the compressional side. Finally, we note that while the aseismic plastic strain accumulation may eventually subside in the later phases of the earthquake cycle, its effect on the stress redistribution may be long-lived. For example, aseismic plasticity is negligible before the eighth event but we still observe co-seismic plastic strain accumulation on the compression side of the fault during that event. This underscores the critical role in tracking the long-term evolution of stresses and deformation on and off the fault due to the nature of coupling and history dependence of the inelastic processes.

Finally, Figure 8a-c illustrates the slip rate contours for both aseismic and co-seismic periods of the earthquake cycle for the first eight events. For the reference elastic case, shown in Figure 8a the first event is symmetric about the center point of the fault $x = 0$. However, this initial symmetric solution is unstable to numerical perturbations and the nucleation of subsequent events is shifted to the right closer to the rheological transition between the velocity strengthening and velocity weakening patches. Figure 8b shows case (I) with visco-plastic off-fault rheology and $c = 47$ (MPa). We observe this for the high cohesion case, the overall response remains very similar to the elastic case with minor variations in the peak slip rate values. Plasticity accumulation during dynamic rup-

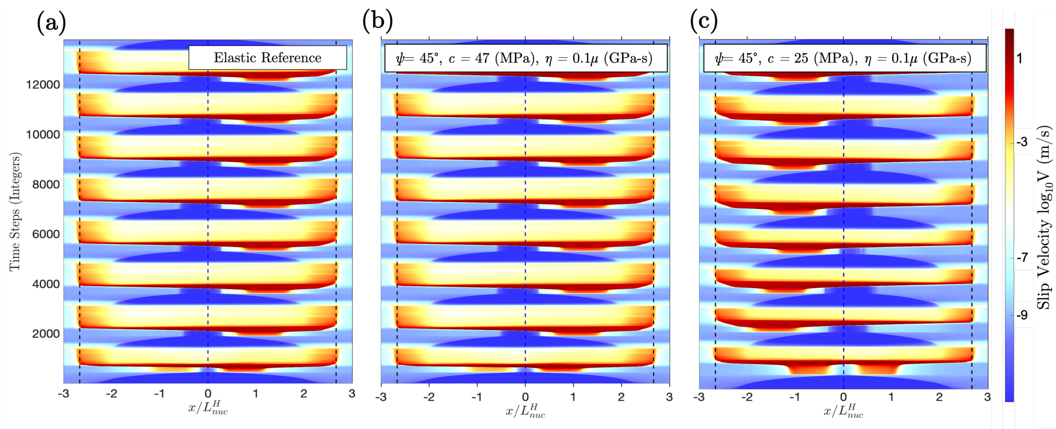

Figure 8. Sequences of earthquakes and aseismic slip for a bulk with visco-plastic rheology versus one that is linear elastic. (a) Time history of the slip rate contours in the elastic case. The sequence of earthquakes is periodic. (b) Time history of the slip rate contours for case (I) with cohesion $c = 47$ (MPa). The plasticity accumulation affects the seismic pattern minimally. (c) Time history of the slip rate contours for case (II) with cohesion $c = 25$ (MPa). The aseismic plastic deformations result in emergence of initial complexity in the earthquake cycle with varying nucleation sites, smaller nucleation size, and irregular seismic pattern rather than periodicity of individual events as in the elastic case. In the contour plots, the fault length is normalized by the nucleation size, time is given by simulation time steps, and the outermost dashed black lines indicate the onset of the creeping regions.

ture introduces a dissipative mechanism that slightly limits the evolution of peak slip rate. Figure 8c shows case (II) with visco-plastic off-fault rheology and $c = 25$ (MPa). The lower cohesion contributes to inelastic strain accumulation during the aseismic phases, which affects the nucleation process of the earthquake events. Accordingly, we observe the emergence of irregular pattern during the first few events of the sequence. This irregularity manifests primarily in the nucleation process where the nucleation size and location vary across the first four events. Apparently, this irregular pattern is limited only to the initial stages of the earthquake cycle in association with the increased aseismic plastic strain accumulation during that period as shown in Figure 6d-f. Beyond the first four events the earthquakes converge to a statistical steady state of periodic events similar to case (I) although the details of the dynamic rupture and plastic strain accumulation remain different as discussed in the previous sections.

Figure 9a-d expands on the above discussion by demonstrating the accumulation of slip for the first eight events comparing case (I) and case (II). For case (I) with larger cohesion, shown in Figure 9a, the fault experiences a sequence of periodic events that nucleates on the right portion of the fault, and propagate primarily to the left edge of the VW segment. Focusing on the zoomed-in Figure 9b, during the first event we observe slight slip deficit accumulation as rupture propagates (highlighted in 9b with black arrow). This slip deficit corresponds to the extent of the plastic strain accumulation in the first event. It reflects the fact that with off-fault plasticity the deformation is partitioned between slip on the fault and inelasticity in the bulk. Case (II), with lower cohesion, experience a more complex behavior during the early stages of the earthquake cycle. The nucleation sites and size change as the off-fault material experience plastic strain accumulation during the aseismic portion of the cycle as shown in Figure 9c. Similar to case (I) we observe signatures of slip irregularities that occur as inelastic strains

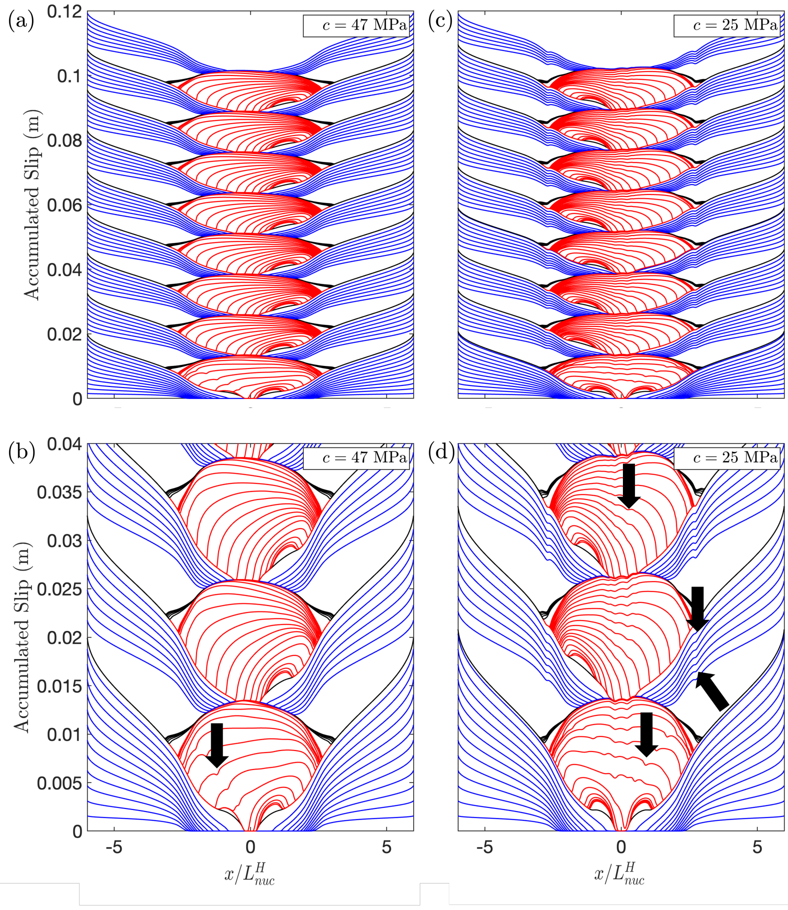

Figure 9. A comparison of slip accumulation for case (I) with cohesion $c = 47$ (MPa) vs slip accumulation for case (II) with cohesion $c = 25$ (MPa). Slip during aseismic period (blue) is plotted every 0.05 years. Slip during the coseismic period (red) is plotted every 0.001 s. Slip during intermediate stages (black) is plotted every 10 s. (a) Slip contours for case (I) showing smooth slip accumulation profile with minimal slip deficit generated during the dynamic rupture phases of the earthquake cycle. (b) Slip contours for case (II) showing the accumulation of slip deficit within the creeping regions of the fault, as well as, during the dynamic rupture phases, due to the partitioning of deformation between on-fault slip and off-fault plastic strain. Furthermore, the accumulation of off-fault plastic strains during the aseismic period results in an initially complex seismic pattern.

are accumulated during dynamic rupture (shown in Figure 9d). Moreover, we observe slip deficits in the creeping region of the fault. Overall, the slip profile for case (II) shows a rougher slip accumulation along the fault compared to the smoother profile observed for case (I).

5 Discussion

We have developed an efficient framework to account for off-fault plastic response for sequence of earthquakes and aseismic slip for 2-D half-spaces separated by a rate-and-state planar fault. The proposed computational framework account for inertial effects during coseismic phases of the earthquake cycle, hence, incorporating the role of wave-madiated stress transfer on the off-fault plastic deformations during dynamic rupture. We considered a Drucker-Prager model and introduced a visco-plastciity formulation for numerical regularization.

Our framework couples finite element (FEM) with a spectral boundary integral equation (SBIE) methods allowing for computational domain truncation without loss of accuracy. The incorporation of finite element allows for the inclusion of material nonlinearity, such as viscoplasticity, within a finite-width strip while still benefiting from the computational efficiency of spectral boundary integral approach in handling the exterior half spaces. Additionally, the incorporation of SBIE enables the modeling of unbounded domains. Prior to this work, off-fault plasticity has been considered in the context of SEAS using domain based approaches, resorting to extreme domain truncation (e.g. a strip-like model), imperfect absorbing boundaries, or modeling purely quasi-dynamic behavior to reduce the computational cost. While the prior studies have provided important insights into the potential effects of nonlinear rheology on the seismic response, different approximations adopted previously might have introduced artifacts that influenced the conclusions. For example, the static stress field in a strip-like model is substantially different from the static stress field in an unbounded domain and this may be important for modeling aseismic deformation. Imperfect absorbing boundary condition, especially if imposed close to the fault, may introduce artificial wave reflections that influence the dynamic rupture characteristics as well as the plastic strain accumulation. A purely quasi-dynamic approach neglects wave-mediated stress transfer and may result in lower peak slip rates and rupture propagation speeds which in turn may qualitatively change the off-fault plastic strain accumulation. The framework described in this paper provides a step towards an integrated methodology that could potentially alleviate some of the restrictions associated with domain-based modeling.

For this initial study, the application of our algorithm has had two main themes: (i) exploring how the initial angle of maximum compressive principal stress Ψ affects the accumulation of inelastic strains, and consequently the fault response, and (ii) investigating how altering the yield stress through varying the cohesion influences the fault response through plasticity accumulation within the different phases of the earthquake cycle. Both themes have been explored before in the context of single dynamic rupture simulations (Templeton & Rice, 2008; Dedontney et al., 2011; Dunham et al., 2011). A major contribution of this paper is revisiting this problem within the framework of earthquake sequence modeling to assess the role of co-evolution of fault slip and off-fault plasticity on the characteristic of seismic and aseismic slip over long time scales independent of the initial state.

For the four different Ψ values at relatively high yield stress with $c = 47$ (MPa), our simulations reveal that inelastic strain primarily accumulates during dynamic rupture when the deformation gradients are sufficiently sharp enough at the crack tip to allow for the onset of yielding. The location and magnitude of the plastic strain change as we vary Ψ. Particularly, the plasticity accumulation occurs at the extensional side for $\Psi = 45°, 35°, 25°$, and the magnitude decrease as Ψ decrease. Initial studies by (Andrews, 2005; Duan, 2008) on off-fault co-seismic plasticity accumulation suggested that for $\Psi = 45°$ inelastic deformations are localized with the extensional side of the fault. (Templeton & Rice, 2008; Dunham et al., 2011) later demonstrated that the initial choice of Ψ alters the location of plasticity, and that at lower $\Psi \leq 25$ inelastic deformations are observed in the congressional side. In the context of SEAS, (Tal & Faulkner, 2022) studied the plasticity accumulation for planar and rough faults using a domain-based approach on a smaller domain considering $\Psi = 45°$ and demonstrated plasticity accumulation in the extensional side of the fault during the dynamic rupture phases of the simulations. Thus, in the absence of aseismic plasticity accumulation, our results are in a qualitative agreement with previous studies of single dynamic ruptures and a special class of SEAS models (Tal & Faulkner, 2022).

However, our findings related to the influence of aseismic plastic strain accumulation, in the case with lower cohesion $c = 25$ (MPa) are particularly novel in the sense that previous studies have considered yielding to occur only when the slip rate is sufficiently large. Here, we observe spontaneous evolution of off-fault plasticity during both seismic and aseismic phases. The aseismic plasticity observed in this study is due to the stress concentration associated with aseismic slip creeping into the locked regions of the fault. At lower cohesion values, plasticity may accumulate aseismically while the slip rate is low and this strongly influenced the the earthquake cycle and subsequent co-seismic plastic strain accumulation. For the set of parameters we considered in this study, we observe that aseismic plasticity may be limited to the early stages of the earthquake cycle. Nonetheless, this aseismic plastic strain accumulation produce persistent underlying stress heterogeneity that cause the inelastic deformations during dynamic phases to deviate from traditional damage patterns observed in individual dynamic rupture simulations. Mainly, we observe that plasticity may accumulate in both extensional and compressional sides of the off-fault bulk even at $\Psi = 45°$. Furthermore, the evolution of the plastic strain and depletion of plasticity later in the cycle suggests that it is important to consider the full deformation history before modeling plasticity in a given event. This is not surprising since plasticity is a history-dependent process.

In this initial study, we have focused on viscoplasticity as an idealization of isotropic densely distributed microcracking in the rock mass. However, more comprehensive constitutive modeling frameworks for quasi-brittle damage exist and may be more appropriate for modeling inelastic processes in fault zones. For example, we have not considered the well-documented feedback between damage accumulation and healing and changes in the elastic wave speed. Such feedback may be captured using continuum damage models (Thomas & Bhat, 2018; Xu et al., 2015; Lyakhovsky et al., 1997; Hamiel et al., 2004; Lyakhovsky et al., 2016; Kurzon et al., 2019). Damage formulations bring additional computational complexity for SEAS modeling. Thus, efficient algorithms such as FEBE may offer an attractive tool in handling them in the future compared to the computationally taxing domain-based approaches. Ultimately, rock damage emerge due to a combination of discrete and continuum processes operating at different scales and resulting in damage distributions with different levels of anisotropy(Ma & Elbanna, 2019; Ben-Zion & Sammis, 2003). Modeling this complex evolutionary system will be the focus of future research.

Future extensions of this work may include exploring the implication of off-fault inelastic strain accumulation on fault maturity. Moreover, incorporating complex fault topologies including nonplanar faults as well as branched fault systems, are important next steps.

6 Conclusion

We present an efficient algorithm for modeling earthquake simulations of sequences of earthquakes and aseismic slip in 2-D inplane setting with off-fault viscoplastic rheology. The main conclusions are summarized as follows:

1. For models with higher yield strength, plasticity accumulation occurs during the dynamic rupture phase and primarily localize in the extensional side for larger values of the angle of most compressive stress, $25° \leq \Psi \leq 45°$, but it shifts to accumulate mainly on the compressional side for $\Psi = 15°$.
2. Increasing the closeness to failure by reducing cohesion leads to the accumulation of off-fault inelasticity beyond the co-seismic phase and during the aseismic slip.
3. For $\Psi = 45°$ and lower cohesion, co-seismic plastic strain accumulates in both the extensional and compressional sides of the fault. The unexpected accumulation on the compression side is due to the residual normal stress changes resulting from aseismic creep and off-fault plastic deformations during the interseismic period.
4. For the parameters investigated in this work, plasticity accumulation during aseismic phases was found to be limited to the first few events in the seismic cycle. During that period, aseismic plasticity impacts both the earthquake hypocenter location and nucleation size.
5. Even in the cases where aseismic plasticity becomes negligible later in the sequence, its impact on normal stress redistribution in the bulk is long-lived and may persistently influence the co-seismic plastic strain distribution leading to plasticity patterns that may contrast what is typically observed in simulations of individual dynamic ruptures.

Acknowledgments
The authors acknowledge support from the Southern California Earthquake Center through a collaborative agreement between NSF. Grant Number: EAR0529922 and USGS. Grant Number: 07HQAG0008 and the National Science Foundation CAREER award No. 1753249 for modeling complex fault zone structures. This material is based upon work supported by the Department of Energy under Award Number DE-FE0031685.

Data Availability Statement

The data generated using the numerical algorithm corresponding to this study is available at https://doi.org/10.5281/zenodo.6415071.

References

Aagaard, B. T., Knepley, M. G., & Williams, C. A. (2013). A domain decomposition approach to implementing fault slip in finite-element models of quasi-static and dynamic crustal deformation. *Journal of Geophysical Research: Solid Earth*, *118*(6), 3059–3079. doi: 10.1002/jgrb.50217

Abdelmeguid, M., Ma, X., & Elbanna, A. (2019, 12). A Novel Hybrid Finite Element-Spectral Boundary Integral Scheme for Modeling Earthquake Cycles: Application to Rate and State Faults With Low-Velocity Zones. *Journal of Geophysical Research: Solid Earth*, *124*(12), 12854–12881. doi: 10.1029/2019JB018036

Albertini, G., Elbanna, A. E., & Kammer, D. S. (2021, 12). A three-dimensional hybrid finite element — spectral boundary integral method for modeling earthquakes in complex unbounded domains. *International Journal for Numerical Methods in Engineering*, *122*(23), 6905–6923. doi: 10.1002/nme.6816

Aliabadi, M. H. (1997). Boundary Element Formulations in Fracture Mechanics. *Applied Mechanics Reviews*, *50*(2), 83. Retrieved from `http://appliedmechanicsreviews.asmedigitalcollection.asme.org/article.aspx?articleid=1395876` doi: 10.1115/1.3101690

Allison, K. L., & Dunham, E. M. (2018). Earthquake cycle simulations with rate-and-state friction and power-law viscoelasticity. *Tectonophysics*, *733*(November 2017), 232–256. Retrieved from `https://doi.org/10.1016/j.tecto.2017.10.021` doi: 10.1016/j.tecto.2017.10.021

Ampuero, J. P., & Ben-zion, Y. (2008). Cracks, pulses and macroscopic asymmetry of dynamic rupture on a bimaterial interface with velocity-weakening friction. *Geophysical Journal International*, *173*(2), 674–692. doi: 10.1111/j.1365-246X.2008.03736.x

Ampuero, J.-P., & Rubin, A. M. (2008, 1). Earthquake nucleation on rate and state faults – Aging and slip laws. *Journal of Geophysical Research*, *113*(B1), B01302. Retrieved from `http://doi.wiley.com/10.1029/2007JB005082` doi: 10.1029/2007JB005082

Andrews, D. J. (2005). Rupture dynamics with energy loss outside the slip zone. *Journal of Geophysical Research: Solid Earth*, *110*(1), 1–14. doi: 10.1029/2004JB003191

Barbot, S. (2018). Asthenosphere Flow Modulated by Megathrust Earthquake Cycles. *Geophysical Research Letters*, *45*(12), 6018–6031. doi: 10.1029/2018GL078197

Barbot, S. (2019a). Modulation of fault strength during the seismic cycle by grain-size evolution around contact junctions. *Tectonophysics*, *765*(May), 129–145. Retrieved from `https://doi.org/10.1016/j.tecto.2019.05.004` doi: 10.1016/j.tecto.2019.05.004

Barbot, S. (2019b, 10). Slow-slip, slow earthquakes, period-two cycles, full and partial ruptures, and deterministic chaos in a single asperity fault. *Tectonophysics*, *768*. doi: 10.1016/j.tecto.2019.228171

Ben-Zion, Y., & Sammis, C. G. (2003). Characterization of fault zones. *Pure and Applied Geophysics*, *160*(3-4), 677–715. doi: 10.1007/PL00012554

Biemiller, J., & Lavier, L. (2017, 4). Earthquake supercycles as part of a spectrum of normal fault slip styles. *Journal of Geophysical Research: Solid Earth*, *122*(4), 3221–3240. doi: 10.1002/2016JB013666

Bizzarri, A. (2011, 8). ON THE DETERMINISTIC DESCRIPTION OF EARTHQUAKES. *Reviews of Geophysics*, *49*(3), RG3002. Retrieved from `http://writenowmedia.com/Web_files/MathisBrothers-CompanyStory.pdfhttp://doi.wiley.com/10.1029/2011RG000356` doi: 10.1029/2011RG000356

Breitenfeld, M. S., & Geubelle, P. H. (1998). Numerical analysis of dynamic debonding under 2D in-plane and 3D loading. In *Recent advances in fracture mechanics* (pp. 13–37). Dordrecht: Springer Netherlands. Retrieved from `http://link.springer.com/10.1007/978-94-017-2854-6_2` doi: 10.1007/978-94-017-2854-6{_}2

Cochard, A., & Rice, J. R. (2000, 11). Fault rupture between dissimilar materials: Ill-posedness, regularization, and slip-pulse response. *Journal of Geophysical Research: Solid Earth*, *105*(B11), 25891–25907. Retrieved from `http://doi.wiley.com/10.1029/2000JB900230` doi: 10.1029/2000JB900230

Courant, R., Friedrichs, K., & Lewy, H. (1928, 12). Über die partiellen Differenzengleichungen der mathematischen Physik. *Mathematische Annalen*, *100*(1), 32–74. Retrieved from `http://link.springer.com/10.1007/BF01448839` doi: 10.1007/BF01448839

D'Amico, S. (2016). *Earthquakes and Their Impact on Society* (S. D'Amico, Ed.). Cham: Springer International Publishing. Retrieved from `http://link.springer.com/10.1007/978-3-319-21753-6` doi: 10.1007/978-3-319-21753-6

Day, S. M., Dalguer, L. A., Lapusta, N., & Liu, Y. (2005). Comparison of finite difference and boundary integral solutions to three-dimensional spontaneous rupture. *Journal of Geophysical Research: Solid Earth*, *110*(12), 1–23. doi: 10.1029/2005JB003813

Dedontney, N., Rice, J. R., & Dmowska, R. (2011). Influence of material contrast on fault branching behavior. *Geophysical Research Letters*, *38*(14), 1–5. doi: 10.1029/2011GL047849

Dieterich, J. H. (1979). Modeling of rock friction 1. Experimental results and constitutive equations. *Journal of Geophysical Research: Solid Earth*, *84*(B5), 2161–2168. doi: 10.1029/JB084iB05p02161

Dieterich, J. H. (1992). Earthquake nucleation on faults with rate-and state-dependent strength. *Tectonophysics*, *211*(1-4), 115–134. doi: 10.1016/0040-1951(92)90055-B

Duan, B. (2008, 7). Asymmetric off-fault damage generated by bilateral ruptures along a bimaterial interface. *Geophysical Research Letters*, *35*(14). doi: 10.1029/2008GL034797

Dunham, E. M., Belanger, D., Cong, L., & Kozdon, J. E. (2011). Earthquake ruptures with strongly rate-weakening friction and off-fault plasticity, part 1: Planar faults. *Bulletin of the Seismological Society of America*, *101*(5), 2296–2307. doi: 10.1785/0120100075

Duru, K., Allison, K. L., Rivet, M., & Dunham, E. M. (2019, 7). Dynamic Rupture and Earthquake Sequence Simulations Using the Wave Equation in Second-Order Form. *Geophysical Journal International*, 1–34. Retrieved from `https://academic.oup.com/gji/advance-article/doi/10.1093/gji/ggz319/5533327` doi: 10.1093/gji/ggz319

Erickson, B. A., & Dunham, E. M. (2014). An efficient numerical method for earthquake cycles in heterogeneous media: Alternating subbasin and surface-rupturing events on faults crossing a sedimentary basin. *Journal of Geophysical Research: Solid Earth*, *119*(4), 3290–3316. doi: 10.1002/2013JB010614

Erickson, B. A., & Jiang, J. (2018). *SEAS Benchmark Problem BP1.* Retrieved from `http://scecdata.usc.edu/cvws/seas/`

Freund, L. B. (1979). The mechanics of dynamic shear crack propagation. *Journal of Geophysical Research: Solid Earth*, *84*(B5), 2199–2209. doi: 10.1029/JB084iB05p02199

Geubelle, P., & Rice, J. R. (1995, 11). A spectral method for three-dimensional elastodynamic fracture problems. *Journal of the Mechanics and Physics of Solids*, *43*(11), 1791–1824. Retrieved from `https://linkinghub.elsevier.com/retrieve/pii/002250969500043I` doi: 10.1016/0022-5096(95)00043-I

Geubelle, P. H., & Breitenfeld, M. S. (1997). Numerical analysis of dynamic debonding under anti-plane shear loading. *International Journal of Fracture*, *85*(3), 265–282. doi: https://doi.org/10.1023/A:1007498300031

Hamiel, Y., Liu, Y., Lyakhovsky, V., Ben-Zion, Y., & Lockner, D. (2004). A viscoelastic damage model with applications to stable and unstable fracturing. *Geophysical Journal International*, *159*(3), 1155–1165. doi: 10.1111/j.1365-246X.2004.02452.x

Herrendörfer, R., Gerya, T., & van Dinther, Y. (2018, 6). An Invariant Rate- and State-Dependent Friction Formulation for Viscoeastoplastic Earthquake Cycle Simulations. *Journal of Geophysical Research: Solid Earth*, *123*(6), 5018–5051. doi: 10.1029/2017JB015225

Hillers, G., Ben-Zion, Y., & Mai, P. M. (2006). Seismicity on a fault controlled by rate- and state-dependent friction with spatial variations of the critical slip distance. *Journal of Geophysical Research: Solid Earth*, *111*(1), 1–23. doi: 10.1029/2005JB003859

Jiang, J., Erickson, B. A., Lambert, V. R., Ampuero, J., Ando, R., Barbot, S. D., … Dinther, Y. (2022, 3). Community-Driven Code Comparisons for Three-

Dimensional Dynamic Modeling of Sequences of Earthquakes and Aseismic Slip. *Journal of Geophysical Research: Solid Earth*, *127*(3). Retrieved from https://onlinelibrary.wiley.com/doi/10.1029/2021JB023519 doi: 10.1029/2021JB023519

Kaneko, Y., Ampuero, J.-P., & Lapusta, N. (2011, 10). Spectral-element simulations of long-term fault slip: Effect of low-rigidity layers on earthquake-cycle dynamics. *Journal of Geophysical Research*, *116*(B10), B10313. Retrieved from http://doi.wiley.com/10.1029/2011JB008395 doi: 10.1029/2011JB008395

Kaneko, Y., Lapusta, N., & Ampuero, J.-P. (2008, 9). Spectral element modeling of spontaneous earthquake rupture on rate and state faults: Effect of velocity-strengthening friction at shallow depths. *Journal of Geophysical Research*, *113*(B9), B09317. Retrieved from http://doi.wiley.com/10.1029/2007JB005553 doi: 10.1029/2007JB005553

Kuna, M. (2013). *Finite Elements in Fracture Mechanics* (Vol. 201). Dordrecht: Springer Netherlands. Retrieved from http://link.springer.com/10.1007/978-94-007-6680-8 doi: 10.1007/978-94-007-6680-8

Kurzon, I., Lyakhovsky, V., & Ben-Zion, Y. (2019). Dynamic Rupture and Seismic Radiation in a Damage–Breakage Rheology Model. *Pure and Applied Geophysics*, *176*(3), 1003–1020. doi: 10.1007/s00024-018-2060-1

Lapusta, N., & Liu, Y. (2009). Three-dimensional boundary integral modeling of spontaneous earthquake sequences and aseismic slip. *Journal of Geophysical Research: Solid Earth*, *114*(9), 1–25. doi: 10.1029/2008JB005934

Lapusta, N., & Rice, J. R. (2003, 4). Nucleation and early seismic propagation of small and large events in a crustal earthquake model. *Journal of Geophysical Research: Solid Earth*, *108*(B4), 1–18. Retrieved from http://doi.wiley.com/10.1029/2001JB000793 doi: 10.1029/2001JB000793

Lapusta, N., Rice, J. R., Ben-Zion, Y., & Zheng, G. (2000, 10). Elastodynamic analysis for slow tectonic loading with spontaneous rupture episodes on faults with rate- and state-dependent friction. *Journal of Geophysical Research: Solid Earth*, *105*(B10), 23765–23789. Retrieved from http://doi.wiley.com/10.1029/2000JB900250 doi: 10.1029/2000JB900250

Lay, T. (2012). Seismology: Why giant earthquakes keep catching us out. *Nature*, *483*(7388), 149–150. doi: 10.1038/483149a

Lewis, M. A., & Ben-Zion, Y. (2010, 12). Diversity of fault zone damage and trapping structures in the Parkfield section of the San Andreas Fault from comprehensive analysis of near fault seismograms. *Geophysical Journal International*, *183*(3), 1579–1595. Retrieved from https://academic.oup.com/gji/article-lookup/doi/10.1111/j.1365-246X.2010.04816.x doi: 10.1111/j.1365-246X.2010.04816.x

Liu, Y., & Rice, J. R. (2007, 9). Spontaneous and triggered aseismic deformation transients in a subduction fault model. *Journal of Geophysical Research*, *112*(B9), B09404. Retrieved from http://doi.wiley.com/10.1029/2007JB004930 doi: 10.1029/2007JB004930

Luo, Y., & Ampuero, J.-P. (2018, 5). Stability of faults with heterogeneous friction properties and effective normal stress. *Tectonophysics*, *733*(October 2017), 257–272. Retrieved from https://doi.org/10.1016/j.tecto.2017.11.006https://linkinghub.elsevier.com/retrieve/pii/S0040195117304596 doi: 10.1016/j.tecto.2017.11.006

Lyakhovsky, V., Ben-Zion, Y., & Agnon, A. (1997). Distributed damage, faulting, and friction. *Journal of Geophysical Research B: Solid Earth*, *102*(12), 27635–27649. doi: 10.1029/97jb01896

Lyakhovsky, V., Ben-Zion, Y., Ilchev, A., & Mendecki, A. (2016, 8). Dynamic rupture in a damage-breakage rheology model. *Geophysical Journal International*, *206*(2), 1126–1143. Retrieved from https://academic.oup.com/gji/article

-lookup/doi/10.1093/gji/ggw183 doi: 10.1093/gji/ggw183

Ma, X., & Elbanna, A. (2019, 10). Dynamic rupture propagation on fault planes with explicit representation of short branches. *Earth and Planetary Science Letters*, *523*, 115702. Retrieved from https://linkinghub.elsevier.com/retrieve/pii/S0012821X19303887 doi: 10.1016/j.epsl.2019.07.005

Ma, X., Hajarolasvadi, S., Albertini, G., Kammer, D. S., & Elbanna, A. E. (2018, 1). A hybrid finite element-spectral boundary integral approach: Applications to dynamic rupture modeling in unbounded domains. *International Journal for Numerical and Analytical Methods in Geomechanics*, *43*(1), 317–338. Retrieved from https://onlinelibrary.wiley.com/doi/abs/10.1002/nag.2865 doi: 10.1002/nag.2865

Mckay, M. B., Erickson, B. A., & Kozdon, J. E. (2019). A Computational Method for Earthquake Cycles within Anisotropic Media. *Geophysical Journal International*, 816–833. doi: 10.1093/gji/ggz320

Okubo, P. G. (1989). Dynamic rupture modeling with laboratory-derived constitutive relations. *Journal of Geophysical Research*, *94*(B9), 12321. Retrieved from http://doi.wiley.com/10.1029/JB094iB09p12321 doi: 10.1029/JB094iB09p12321

Ranjith, K., & Rice, J. R. (2001). *Slip dynamics at an interface between dissimilar materials* (Vol. 49; Tech. Rep.). Retrieved from www.elsevier.com/locate/jmps

Rice, J. R. (1993). Spatio-temporal complexity of slip on a fault. *Journal of Geophysical Research*, *98*(B6), 9885–9907. doi: 10.1029/93JB00191

Rice, J. R., & Ben-Zion, Y. (1996, 4). Slip complexity in earthquake fault models. *Proceedings of the National Academy of Sciences*, *93*(9), 3811–3818. Retrieved from http://www.pnas.org/cgi/doi/10.1073/pnas.93.9.3811 doi: 10.1073/pnas.93.9.3811

Rice, J. R., & Ruina, A. L. (1983). Stability of Steady Frictional Slipping. *Journal of Applied Mechanics*, *50*(2), 343. Retrieved from http://appliedmechanics.asmedigitalcollection.asme.org/article.aspx?articleid=1406945 doi: 10.1115/1.3167042

Ruina, A. (1983). Slip instability and state variable friction laws. *Journal of Geophysical Research*, *88*(B12), 10359–10370. doi: 10.1029/JB088iB12p10359

Shibazaki, B., & Matsu'ura, M. (1992, 6). Spontaneous processes for nucleation, dynamic propagation, and stop of earthquake rupture. *Geophysical Research Letters*, *19*(12), 1189–1192. Retrieved from http://doi.wiley.com/10.1029/92GL01072 doi: 10.1029/92GL01072

Taborda, R., & Bielak, J. (2011). Large-Scale Earthquake simulation: Computational seismology and complex engineering systems. *Computing in Science and Engineering*, *13*(4), 14–26. doi: 10.1109/MCSE.2011.19

Tal, Y., & Faulkner, D. (2022, 1). The Effect of Fault Roughness and Earthquake Ruptures on the Evolution and Scaling of Fault Damage Zones. *Journal of Geophysical Research: Solid Earth*, *127*(1). doi: 10.1029/2021jb023352

Tal, Y., Rubino, V., Rosakis, A. J., & Lapusta, N. (2020, 9). Illuminating the physics of dynamic friction through laboratory earthquakes on thrust faults. *Proceedings of the National Academy of Sciences*, *117*(35), 21095–21100. Retrieved from http://www.pnas.org/lookup/doi/10.1073/pnas.2004590117 doi: 10.1073/pnas.2004590117

Templeton, E. L., & Rice, J. R. (2008). Off-fault plasticity and earthquake rupture dynamics: 1. Dry materials or neglect of fluid pressure changes. *Journal of Geophysical Research: Solid Earth*, *113*(9), 1–19. doi: 10.1029/2007JB005529

Thakur, P., Huang, Y., & Kaneko, Y. (2020). Effects of Low-Velocity Fault Damage Zones on Long-Term Earthquake Behaviors on Mature Strike-Slip Faults. *Journal of Geophysical Research: Solid Earth*, *125*(8), 1–20. doi: 10.1029/2020JB019587

Thomas, M. Y., & Bhat, H. S. (2018). Dynamic evolution of off-fault medium during an earthquake: A micromechanics based model. *Geophysical Journal International*, *214*(2), 1267–1280. doi: 10.1093/GJI/GGY129

Tong, X., & Lavier, L. L. (2018, 12). Simulation of slip transients and earthquakes in finite thickness shear zones with a plastic formulation. *Nature Communications*, *9*(1). doi: 10.1038/s41467-018-06390-z

Tse, S. T., & Rice, J. R. (1986). Crustal earthquake instability in relation to the depth variation of frictional slip properties. *Journal of Geophysical Research*, *91*(B9), 9452. Retrieved from `http://doi.wiley.com/10.1029/JB091iB09p09452` doi: 10.1029/JB091iB09p09452

Uphoff, C., May, D. A., & Gabriel, A.-A. (2022). A discontinuous Galerkin method for sequences of earthquakes and aseismic slip on multiple faults using unstructured curvilinear grids. *EarthArXiv*. Retrieved from `https://doi.org/10.31223/X50P8B.` doi: 10.31223/X50627

Van Dinther, Y., Gerya, T. V., Dalguer, L. A., Mai, P. M., Morra, G., & Giardini, D. (2013). The seismic cycle at subduction thrusts: Insights from seismo-thermo- mechanical models. *Journal of Geophysical Research: Solid Earth*, *118*(12), 6183–6202. doi: 10.1002/2013JB010380

Xu, S., Ben-Zion, Y., Ampuero, J.-P., & Lyakhovsky, V. (2015, 5). Dynamic Ruptures on a Frictional Interface with Off-Fault Brittle Damage: Feedback Mechanisms and Effects on Slip and Near-Fault Motion. *Pure and Applied Geophysics*, *172*(5), 1243–1267. Retrieved from `http://link.springer.com/10.1007/s00024-014-0923-7` doi: 10.1007/s00024-014-0923-7

Yang, H., Zhu, L., & Cochran, E. S. (2011, 8). Seismic structures of the Calico fault zone inferred from local earthquake travel time modelling. *Geophysical Journal International*, *186*(2), 760–770. Retrieved from `https://academic.oup.com/gji/article-lookup/doi/10.1111/j.1365-246X.2011.05055.x` doi: 10.1111/j.1365-246X.2011.05055.x

Appendix A Finite Element Method

The fault discontinuity implementation in the FEM is based on the domain decomposition approach outlined in (Aagaard et al., 2013). In this approach, the fault surface is considered to be an interior boundary between two domains with + and − sides. The slip on the fault produces equal and opposite tractions on each of those sides, represented by a Lagrange multiplier. It follows that the weak form representation of this problem is give by:

$$-\int_V \sigma_{ij}\phi_{i,j}dV + \int_{S_T} T_i\phi_i dS - \int_V \rho\ddot{u}_i\phi_i dV - \int_{S_{f^+}} T_i^{f^+}\phi_i dS + \int_{S_{f^-}} T_i^{f^-}\phi_i dS = 0 \quad \text{(A1)}$$

where ϕ is the weighting function. The integral along S_f accounts for the Lagrange multipliers (tractions) on the fault surfaces. $T_i^{f^+} = \sigma_{ij}n_j^+$ and $T_i^{f^-} = \sigma_{ij}n_j^-$ where n_j^+ and n_j^- are the fault normals for the positive and negative sides of the faults respectively. These boundary tractions are associated with the slip constraint on the fault shown in expression (11) and are imposed via Lagrange multipliers.

To account for the coupling between the FEM and SBI equation within the finite element formulation, we proceed as follows. We impose the tractions τ^{SBI} that accounts for the existence of the half-spaces as Neumann boundary conditions for the FEM strip. The value of τ^{SBI} is provided through the SBI formulation as will be discussed shortly. This ensures continuity of traction at the outer interfaces. Since the nodes along the outer interfaces share the same kinematic degrees of freedom between the virtual strip and the adjacent half-space, continuity of displacements is also automatically satisfied. Altogether, this leads to the following system of equations:

$$-\int_V \sigma_{ij}\phi_{i,j}dV + \int_{S^+_{SBI}} \tau_i^{+,SBI}\phi_i dS - \int_{S^-_{SBI}} \tau_i^{-,SBI}\phi_i dS - \int_V \rho\ddot{u}_i\phi_i dV$$
$$-\int_{S_{f+}} T_i^{f^+}\phi_i dS + \int_{S_{f-}} T_i^{f^-}\phi_i dS = 0 \qquad \text{(A2)}$$

$$\int_{S_f} \phi_k \left[R_{ki}(u_i^+ - u_i^-) - \delta_k\right] = 0 \qquad \text{(A3)}$$

Expressions (A1) and (A3) may be discretized using a Galerkin approach. Accordingly, we express the test function ϕ, trial solution u , Lagrange multipliers T^f, fault slip δ_k, and SBI tractions τ^{SBI} as linear combinations of basis function $N(x)$:

$$\phi = \sum_m w_m N_m(x_i), \quad u = \sum_n u_n N_n(x_i), \quad T^f = \sum_p T_p^f N_p(x_i),$$
$$\tau^{SBI} = \sum_s \tau_s^{SBI} N_s(x_i), \quad \delta = \sum_p \delta_p N_p(x_i) \qquad \text{(A4)}$$

The subscripts denote the number of basis functions, where n is the number of functions associated with the domain displacements, p is the number of functions associated with fault surface, m is the number of basis functions for the test solutions, and s denotes the functions associated with the SBI degree of freedoms. In the presented numerical models, linear Lagrange basis functions are utilized for the spatial discretization of the simulated domain. Noting that the tractions on the fault are equal in magnitude, the weak form is transformed into:

$$-\int_V \nabla N_m^T \cdot \sigma(t)dV + \int_{S^+_{SBI}} N_m^T N_{s^+}\tau_{s^+}^{SBI}(t)dS - \int_{S^-_{SBI}} N_m^T N_{s^-}\tau_{s^-}^{SBI}(t)dS$$
$$-\int_{S_{f+}} N_m^T N_p T_p^f(t)dS + \int_{S_{f-}} N_m^T N_p T_p^f dS = \int_V \rho N_m^T N_m dV\,\ddot{u}_n \qquad \text{(A5)}$$

$$\int_{S_f} N_p^T \left[R_{pn}(N_n u_n^+(t) - N_n u_n^-(t)) - N_p\delta_p(t)\right] dS = 0 \qquad \text{(A6)}$$

Assuming that the fault surface is aligned with the domain coordinate system these expressions are converted to a more compact matrix notation as:

$$\mathbf{M}\ddot{u}(t) + \mathbf{K}u(t) + \mathbf{L}_s^T\tau^{SBI}(t) + \mathbf{L}^T T^f(t) = \mathbf{F}(t) \qquad \text{(A7)}$$

$$\mathbf{L}u(t) = \mathbf{D}(t) \qquad \text{(A8)}$$

In this problem, the unknowns are the bulk displacement u_n, the fault tractions (Lagrange multipliers) T^f, and SBI tractions τ^{SBI}. On the fault surface S_f, we prescribe slip δ based on explicit time integration of the slip rate. The fault tractions are then solved for as part of the unknowns in the linear system of equations (A7) and (A8).The fault constitutive law then dictates the dependency of the fault tractions on the slip rate and state variable, which we utilize to solve for the slip rate and march forward in time once we obtain the solution for the fault tractions.

Appendix B Spectral Boundary Integral Method

The boundary integral method has been used extensively since the mid-1980s to study the propagation of cracks (Aliabadi, 1997; Barbot, 2018). The main advantage of this method is that it eliminates the need to study wave propagation in the entire domain by using integral relationships between the displacement discontinuities and tractions along the crack path (Day et al., 2005). The spectral formulation of this method gives an exact form of such a relationship in the Fourier domain. We use the spectral formulation introduced in (P. Geubelle & Rice, 1995), where the elastodynamic analysis of each half-space is carried out separately. In view of the hybrid method, where SBI equation constitutes a boundary condition to the FEM model through tractions τ^{SBI}, we focus the description on modeling a half-space. For brevity, we restrict our discussion to the anti-plane formulation of the SBI scheme. However, we note that the formulation of the independent SBI equation for a three-dimensional (3-D) domain may be readily incorporated in the hybrid scheme (Breitenfeld & Geubelle, 1998). The relationship between the traction τ_i and the resulting displacements at the boundary of a half-space may be expressed as:

$$\tau_i^{\pm}(x_1,t) = \tau_i^{0\pm}(x_1,t) \mp \eta_i \dot{u}_i^{\pm}(x_1,t) \pm f_i^{\pm}(x_1,t) \tag{B1}$$

where, $\tau_i^0(x_1,t)$ is the traction that would be present on the surface, $\pm$ represents upper and lower half plane. $\eta_1 = \mu/c_s$, $\eta_2 = \mu c_p/c_s^2$, where c_s and c_p are the shear and pressure wave speeds respectively. The terms $\eta_i \dot{u}_i$ represent radiation damping. $f_i^{\pm}(x_1,t)$ is a functional given by the space time convolution of the fundamental elastodynamic solution with prior history of slip along the half plane surface. It account for the wave-mediated stress transfer, and is computed in the Fourier domain. For the more interested reader, we refer to (P. Geubelle & Rice, 1995; P. H. Geubelle & Breitenfeld, 1997; Breitenfeld & Geubelle, 1998; Ma et al., 2018).